Please note that this manuscript is a non-peer reviewed preprint submitted to EarthArXiv. It has yet to go through peer-review. Subsequent versions may differ in content from this preprint. If accepted, subsequent versions will be available via the "peer-reviewed Publication DOI' link on the right-hand side of this webpage. Please feel free to contact any of the authors as we welcome feedback on our work.

On the Efficiency and Durability of Ocean Iron Fertilization as a Carbon Dioxide Removal Solution

David A. Siegel[1,2,*], Kana Yamamoto[1] & Timothy DeVries[1,2]

1 - Earth Research Institute, University of California, Santa Barbara
2 - Department of Geography, University of California, Santa Barbara
* - Corresponding author, david.siegel@ucsb.edu

Draft Date: October 9, 2026
Target Journal: *Earth's Future*

Abstract:

Ocean iron fertilization (OIF) is thought to be a promising CO_2 removal (CDR) methodology that can contribute to net negative carbon emission goals. In principle, adding iron to iron-depleted regions of the ocean enhances ocean productivity and the export of organic matter to depth allowing atmospheric CO_2 to invade into the ocean. However, if no carbon is buried on the seafloor, OIF carbon sequestration will be temporary. Furthermore, ocean mixing and subduction of the perturbed dissolved inorganic carbon (DIC) distribution and the relatively slow rates of air-sea gas exchange can alter the efficiency of OIF atmospheric CO_2 uptake. To investigate these processes, we assess the efficiency and durability of OIF CDR using an ocean circulation model coupled to a well-mixed atmosphere. We find that for a typical export flux profile, OIF will be inefficient, with a global mean efficiency relative to direct air capture (DAC) of 24% after 20 years. The inefficiency is driven by ocean mixing and subduction of the DIC perturbation and slow rates of air-sea CO_2 exchange. Deeper penetrating export flux profiles will increase OIF efficiency substantially and global mean efficiencies can approach ~50%. Nonetheless, OIF CDR is durable and most of the CO_2 sequestered after 20 years will remain in the ocean for >100 years. Our work demonstrates that OIF efficiency and durability are determined by a combination of ocean circulation and mixing, the rate of gas exchange and the depth to which the carbon is exported before being remineralized.

Plain Language Summary:

Biological production in the ocean's high nutrient-low chlorophyll (HNLC) regions is limited by the availability of iron and ocean iron fertilization (OIF) experiments in these regions has shown that iron additions can lead to intense phytoplankton blooms. This

has led some to suggest that the purposeful addition of iron in HNLC environments would also enhance the export of organic carbon to depth via sinking particles, enabling atmospheric CO_2 to invade into the ocean and contributing to global CO_2 removal (CDR) goals. Here, we use an ocean-atmosphere transport model to address the efficiency and durability of OIF CDR. We find that for typical organic matter sinking rates, OIF CDR will be inefficient, with efficiency levels four-fold lower than what would be found for direct air capture (DAC). If the sinking fluxes penetrate deeper into the water column, OIF CDR efficiencies can reach up to 50% of DAC. Nonetheless, OIF CDR is durable and most of the CO_2 that is sequestered will remain in the ocean for more than 100 years. Our work demonstrates the limitations and challenges of OIF CDR and suggests future research directions if it is to be considered a viable CDR solution.

Key Points

1. Ocean iron fertilization carbon sequestration is roughly 10-50% as efficient as direct air capture
2. Most of the carbon sequestered by OIF is durable on centennial time scales
3. Vertical mixing, gas exchange & the remineralization profile for sinking carbon biomass regulate OIF efficiency

Keywords: Ocean iron fertilization, carbon dioxide removal (CDR), air-sea gas exchange, ocean circulation and mixing, CDR efficiency and durability

AGU Indices: 1615, 1635, 1627, 4806

CRediT taxonomy: Conceptualization - all authors, Methodology, Software & Visualization - all authors, Writing, original draft - DAS, Writing, review and editing - all authors

1. Introduction

The need to achieve net negative CO_2 emissions to reduce the impacts of global warming has led to proposals for a broad array of CO_2 removal (CDR) approaches (GESAMP, 2019; NASEM, 2019; 2022; Doney et al. 2024; Edwards et al. 2026). Proposed CDR approaches range from direct air capture (DAC) of CO_2 from the atmosphere and its permanent geological storage, to enhancing and restoring the forested regions on the Earth, to increasing alkalinity levels of the surface ocean enabling the oceans to absorb more CO_2. However, the efficiency, durability, economic feasibility, and societal and environmental impacts of many of these CDR approaches remains largely unknown, slowing progress on achieving net negative emission targets (NASEM, 2026).

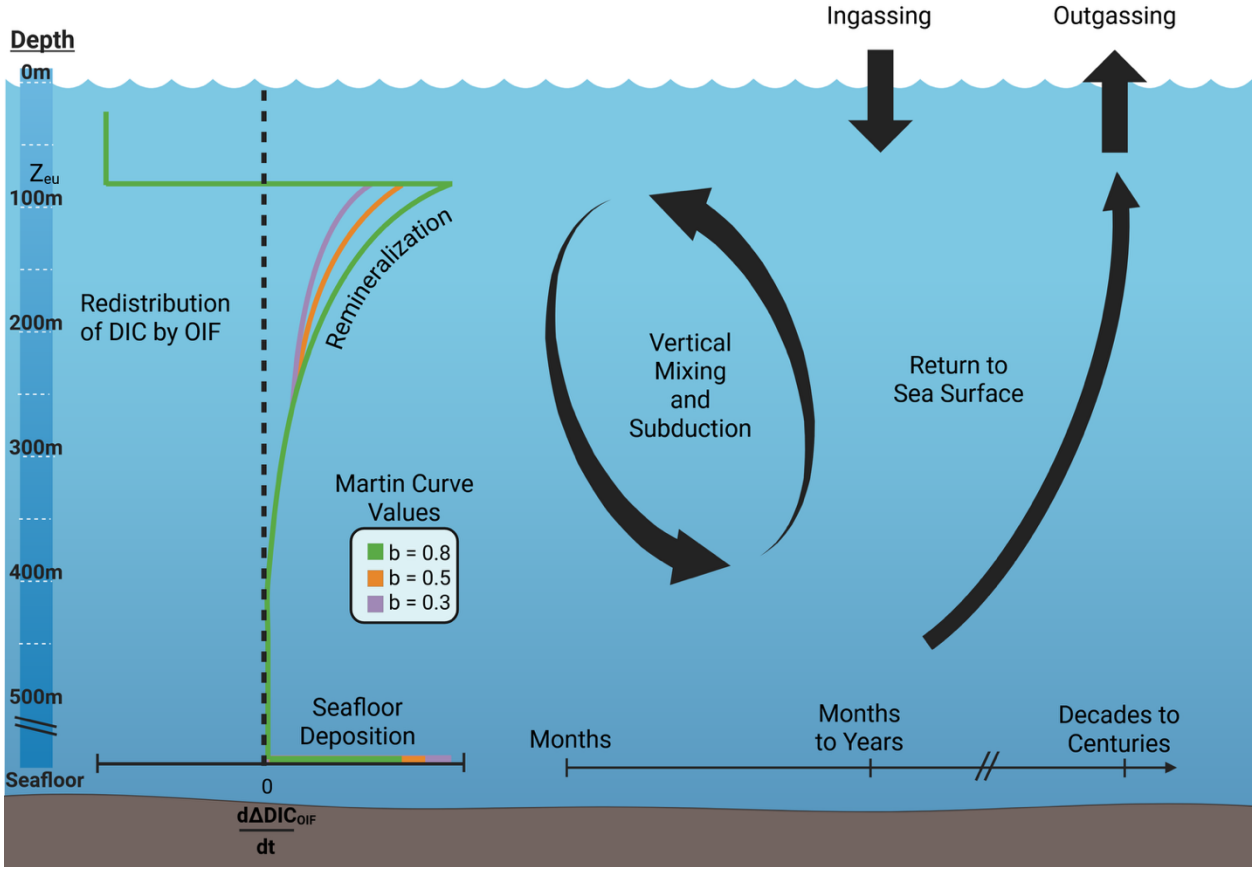


Figure 1: Conceptual diagram of the CO_2 impacts of OIF CDR. Shown on the left is the profile of the redistribution of DIC due to an OIF CDR event in the upper ocean as modeled following equation 2 (see methods). Example shown is for a 5000 m water column and an euphotic zone depth, Z_{eu}, of 80 m for Martin curve b values of 0.3 (purple), 0.5 (orange) and 0.8 (green) with only the upper 500 m shown. The arrows in the middle illustrate the interacting effects of vertical mixing, subduction and the slow air-sea CO_2 exchange on the OIF perturbation. The arrow on the right symbolizes the eventual return of the OIF fixed DIC to the sea surface and its exchange with the atmosphere. The time scales over which these factors operate vary from days to centuries.

Ocean iron fertilization (OIF), the enhancement of ocean productivity and subsequent export of organic matter to depth in iron depleted regions of the ocean, is one possible mCDR solution (NASEM, 2022; Doney et al. 2024; Buesseler et al, 2024). Aeolian iron supply to the oceans has long been hypothesized having a fundamental role in regulating the ocean's biological pump, atmospheric CO_2 concentrations and thereby Earth's radiative forcing and climatic state (Martin, 1990; Jickells et al. 2007). Field experiments have shown a rapid increase in phytoplankton productivity and biomass resulting from the addition of dissolved iron in iron-depleted, high nutrient-low chlorophyll (HNLC) regions (Boyd et al. 2007; Yoon et al. 2018). However, a commensurate increase in the export of sinking particulate organic carbon (POC) fluxes into the ocean interior due to the iron addition has only been documented during the European Iron Fertilization Experiment (EIFEX) in the Southern Ocean (Smetecek et al. 2012).

In principle, the progression of an ocean iron fertilization event in a HNLC region should follow a time course as illustrated in Figure 1. The addition of dissolved iron will spur phytoplankton production within days, increasing the export flux of sinking organic C to depth and reducing the surface layer dissolved inorganic carbon (DIC) concentration. The near-surface DIC deficit created by the OIF intervention induces uptake of atmospheric CO_2 over several months to a year, depending on local air-sea gas exchange rates and the residence time of CO_2-depleted surface waters. The exported organic C will be remineralized back to DIC within the water column or on the seafloor, and this excess DIC will be slowly (over tens to thousands of years) transported back to the surface ocean where it is released to the atmosphere. OIF CDR will be less efficient than an instantaneous and permanent CO_2 removal strategy, such as DAC, due to the relatively slow equilibration of CO_2 with the atmosphere after the initial OIF deployment, the vertical mixing of the OIF induced DIC perturbation and the slow leakage of the temporarily sequestered CO_2 back to the atmosphere. Hence, OIF CDR should be thought of as a temporary vertical rearrangement of the DIC profile.

Here, we assess the efficiency and durability of an OIF CDR perturbation to the global carbon balance using a steady-state data-constrained ocean circulation model that exchanges CO_2 with a well-mixed atmosphere using realistic air-sea exchange physics. We take the effectiveness of the iron addition at stimulating carbon export as a given, and focus solely on assessing the potential efficiency (how much atmospheric CO_2 can be sequestered) and durability (how long will that CO_2 be sequestered) of OIF CDR. The purpose of our study is neither to promote nor condone OIF CDR as a climate mitigation approach, but rather to provide a quantitative assessment of its efficiency and durability to help facilitate future societal decision making.

2. Methods

We investigate the interacting processes regulating OIF CDR efficiency and durability using the coupled atmosphere-ocean model of Yamamoto et al. (2024). The model includes an ocean circulation component that advects and mixes DIC anomalies due to OIF CDR perturbations, and a well-mixed atmosphere that exchanges CO_2 with the ocean using a wind-speed based parameterization. The model's circulation and carbonate chemistry are linearized about the present state enabling the changes in the mass fraction of atmospheric CO_2 ($\Delta xCO_2(t)$) and DIC concentrations within the ocean ($\Delta DIC(t, \boldsymbol{x})$) due to the CDR action to be solved for directly as a function of time *t* and location $\boldsymbol{x}$. By perturbing the ocean's DIC distribution or the atmospheric CO_2 concentration, the response to a variety of CDR approaches can be explored, including direct air capture (DAC) and OIF CDR. Evolution equations for $\Delta xCO_2(t)$ and $\Delta DIC(t, \boldsymbol{x})$ and their derivation are presented in Yamamoto et al. (2024) and in the *Supplemental Materials*.

The model uses a data-assimilated, global ocean circulation inverse model (OCIM), which is an estimate of the modern ocean's steady-state circulation and mixing on annual time scales (DeVries 2014; DeVries and Primeau 2011). Here we use the OCIM2-48L, which has a 2° horizontal resolution and 48 depth levels (Holzer et al. 2021). The atmosphere is represented by a single well-mixed reservoir that exchanges CO_2 with each surface ocean grid cell. Calculations to be presented were performed at each ocean water column where annual mean surface nitrate concentrations are greater than 5 μmol kg^{-1} and annual mean ice cover is less than 50% (Figure S1). Further details of the modeling system and the data sources used are provided in the *Supplemental Materials*.

Yamamoto et al. (2024) defined the relative efficiency of a marine CDR perturbation compared to instantaneous and permanent DAC, $\varepsilon(t, \boldsymbol{x})$, as

$$\varepsilon(t, \boldsymbol{x}) \;=\; \Delta C_{atm,mCDR}(t, \boldsymbol{x}) / \Delta C_{atm,DAC}(t) \qquad (1)$$

where $\Delta C_{atm,mCDR}(t)$ and $\Delta C_{atm,DAC}(t)$ are the changes in the atmospheric concentration of CO_2 due to the same amount of carbon removed from either the atmosphere or ocean, respectively. In this way, $\varepsilon(t,\boldsymbol{x})$ expresses the efficiency and durability of an OIF CDR perturbation relative to a DAC standard (Yamamoto et al. 2024).

One of the goals of CDR in general and for OIF CDR in particular is to sequester atmospheric CO_2 for 100 or more years (NAESM 2021; Buesseler et al. 2024). Using determinations of OIF CDR relative efficiency, an index for the centennial scale durability of OIF CDR can be defined,

$$DI(\boldsymbol{x}) = \frac{\varepsilon(100,\boldsymbol{x})}{\varepsilon(20,\boldsymbol{x})} \qquad (2)$$

If $DI(\boldsymbol{x})$ is equal to one, the relative efficiency of the CDR action has not changed from 20 to 100 years and the atmospheric CO_2 sequestered during the ingassing phase remains in the ocean. However, when $DI(\boldsymbol{x})$ is equal to zero, the initially sequestered CO_2 has all returned to the atmosphere. A value of 20 years after the OIF CDR intervention is chosen for the beginning of the durability index calculation to ensure that the ingassing phase has completed.

OIF CDR induces a vertical redistribution of the local DIC profile as illustrated in Figure 1. The addition of iron to the surface ocean in HNLC regions spurs phytoplankton production, reducing DIC in the euphotic zone and creating organic matter that is transported by biological pump pathways to depth (or deposited on the seafloor), where it is remineralized back to DIC. Thus, to assess the impacts of the OIF CDR action on atmospheric CO_2 concentrations, one needs to know the CDR-induced DIC uptake and remineralization profile. Unfortunately, little is presently known to parameterize this profile. Given the large uncertainties in its specification, we assume that a small amount of DIC, C_o, is removed from the euphotic zone, Z_{eu}, over some period of time, T, and that amount of exported carbon is redistributed beneath Z_{eu} as respired DIC assuming a flux remineralization profile based upon a Martin flux curve (Martin et al. 1987), or

$$F(z) = F_o\,(z/Z_{eu})^{-b} \tag{3}$$

where $F(z)$ is the sinking particle flux as a function of depth, z, F_o is the flux at the base of the euphotic zone (= $C_o\,Z_{eu}\,/\,T$) and b is a metric describing the attenuation of the sinking particle flux with depth (higher values are more rapidly attenuated with depth). The resulting OIF-induced perturbation to the DIC distribution is

$$\frac{dDIC}{dt} = \begin{cases} -C_o/T & z \le Z_{eu} \\ \frac{bC_oZ_{eu}^b}{T}\,z^{-(b+1)} & z > Z_{eu} \end{cases} \tag{4}$$

For each OCIM grid where calculations are made, 0.001 Pg C per year of DIC is removed for one month, mimicking the time scale of a single OIF release. Any sinking flux reaching the bottom OCIM grid depth is remineralized to DIC in the grid cell above the seafloor. The fraction of C_o that reaches the seafloor ranges from a few percent to nearly 50% and is a function of both the bottom depth and the assumed b value (Figure S2). A similar modeling approach has been used previously by Sten et al. (2026) to assess the efficiency and durability of large-scale seaweed cultivation and purposeful sequestration CDR.

The choice of the power law values for the Martin curves, b = 0.8, 0.5 & 0.3, encapsulates the range of observed values (Buesseler et al. 2020). A b value of 0.8 is thought to be a canonical value for the global ocean (Martin et al. 1987; Taylor et al. 2026), while the two smaller (and more deeply penetrating) b values are chosen as it is thought that OIF perturbations should stimulate the growth of large phytoplankton such

as diatoms which are associated with fast-sinking particle fluxes (Smetacek et al. 2012; Yoon et al. 2018; Buesseler et al. 2024).

Several relevant depth scales, the depths for the mixed layer, Z_{ml}, and the euphotic zone, Z_{eu}, are used to help interpret the OIF CDR relative efficiency and durability metrics (Figures S3 & S4). Differences between them will have an immediate bearing on the concentration of the DIC deficit in contact with the atmosphere. For example, if Z_{ml} is deeper than Z_{eu}, then the OIF induced DIC perturbation will mix throughout a deeper mixed layer, diluting the DIC deficit in contact with the atmosphere, thereby reducing the potential atmospheric CO_2 uptake. Whereas if Z_{eu} is deeper than Z_{ml}, the OIF induced DIC deficit will remain in contact with the atmosphere for longer period of time, increasing the atmospheric CO_2 uptake. Differences between Z_{ml} and Z_{eu} show large spatial differences (from roughly -70 to >100 m) in the three major regions where OIF is possible (Figure S5).

Three time scales are also used to help in the interpretation of the OIF CDR efficiency and durability metrics. First, the residence time for water parcels to remain in the mixed layer, $T_{sub}(\boldsymbol{x})$, is calculated (Figure S6). Values of $T_{sub}(\boldsymbol{x})$ are determined as the time it takes for the concentration of a tracer released within the mixed layer to be reduced by a factor of two. Second, the mean time that the remineralized DIC below the euphotic zone from the OIF perturbation remains out of contact with the surface ocean, $T_{ret}(\boldsymbol{x},b)$, is calculated (Figure S7). Values of $T_{ret}(\boldsymbol{x},b)$ are determined as the mean first passage time (Primeau, 2005) for the remineralized DIC beneath the euphotic zone to reach the sea surface and a function of the assumed b value used. Last, the time scale for equilibration of air-sea CO_2 gas exchange, $T_{CO2}(\boldsymbol{x})$, is determined for the surface mixed layer (Figure S8) using equation S4 based upon local carbonate chemistry, mixed layer depth and wind speed (Yamamoto et al. 2024). Further calculation details for these metrics can be found in the Supplementary Materials section.

3. Results

The time dependence of the OIF potential global mean relative efficiency, $\overline{\varepsilon(t,b)}$, provides a useful metric for assessing both the efficiency and durability of OIF CDR (Figure 2). Initially, values of $\overline{\varepsilon(t,b)}$ are zero, and increase for several years thereafter during an ingassing phase as the ocean takes up atmospheric CO_2 due to the surface CO_2 depletion. This is followed by gradual reduction in $\overline{\varepsilon(t,b)}$ as the OIF-sequestered CO_2 returns to the atmosphere. However, the maximum global mean efficiency relative to DAC achieved is moderate, ~50% for the most penetrating flux profile examined (b=0.3); whereas for a canonical sinking flux profile (b=0.8), mean values peak at ~33%. Values of relative efficiency for OIF never approach the near complete efficiency found for instantaneous alkalinity enhancement or direct ocean capture (Bach et al. 2023a; Yamamoto et al. 2024; Zhou et al. 2025).

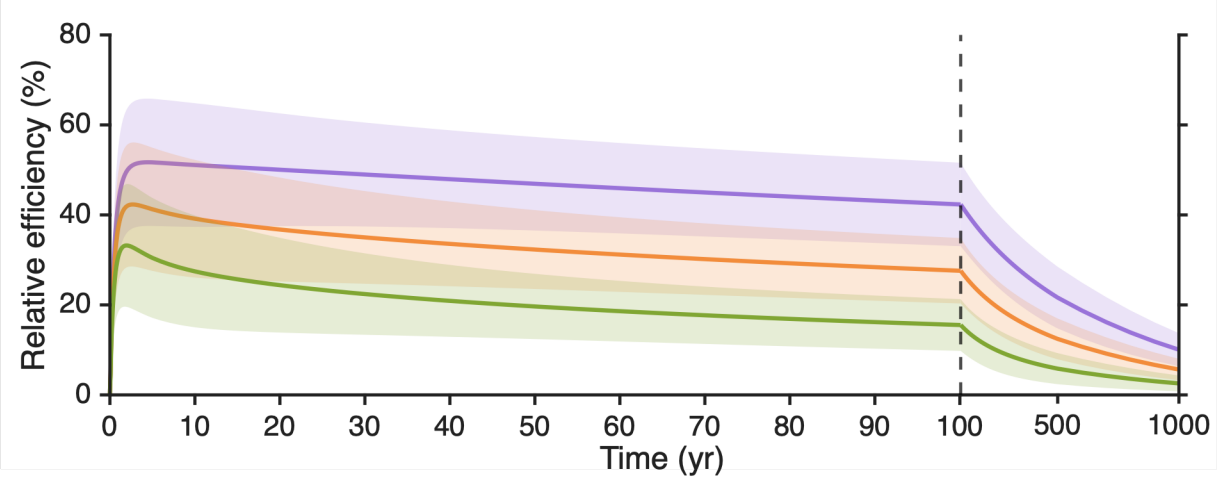


Figure 2. Global mean time courses for the relative efficiency, $\overline{\varepsilon(t,b)}$, vs. time since deployment in years. Values averaged over all ocean surface grids where surface NO_3 values are > 5 μmol kg^{-1} and seasonal ice cover is less than 50%. The colored lines are the mean for Martin 'b' values of 0.3 (purple), 0.5 (orange) and 0.8 (green). The colored envelopes display the spatial standard deviation about the global mean value.

Values of $\overline{\varepsilon(t,b)}$ are strongly dependent on the assumed power law slope of the OIF remineralization profile. Mean values of $\overline{\varepsilon(20,b)}$ are 50, 37 and 24% and for $\overline{\varepsilon(100,b)}$ are 42, 28 and 16% for *b* values of 0.3, 0.5 & 0.8, respectively. The larger the b value, the quicker the sinking particle flux profile is attenuated with depth and the shallower the OIF-induced export of organic carbon penetrates into the ocean interior, decreasing the CO_2 return time and lowering the relative efficiency. Globally, on average 31% (stdev. = 3%) of the OIF CDR perturbation is deposited on the seafloor for the *b*=0.3 case, while only 5% (stdev. = 3%) reaches the seafloor for the *b*=0.8 case (Figure S2). This has an impact on the overall efficiency of OIF CDR due to the longer first passage times for water parcels to traverse from the seafloor to the surface (Siegel et al. 2021).

Although OIF CDR is inherently inefficient, it is fairly durable once the ingassing phase is completed, typically after a few years. Global mean values for the centennial scale durability index ($\overline{DI(b)}$; eq. 3) are 87, 79 and 70% for *b* values of 0.3, 0.5 and 0.8, respectively (Figure 2). The sensitivity of the centennial scale durability index to b value reflects differences in the mean return time for the remineralized biomass to reach the sea surface, which decreases from 107, 63 and 37 years for *b* values of 0.3, 0.5 and 0.8, respectively (Figure S7). This illustrates that although OIF CDR is inefficient relative to DAC, the resulting carbon sequestration can be durable for many decades, especially for cases where the OIF flux remineralization occurs deeper in the water column (low *b* values).

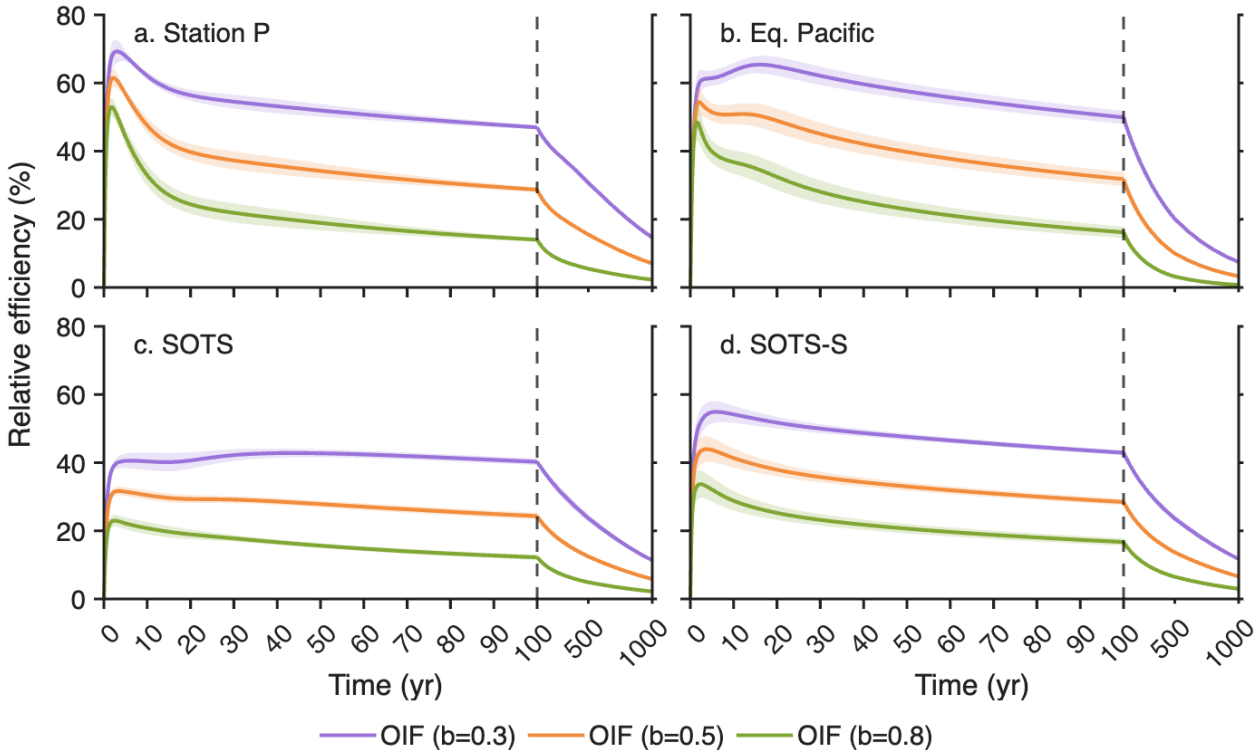


Figure 3. Determinations of time courses of relative efficiency for four HNLC sites where OIF CDR could be conducted: a) Station P in the northeastern Pacific (centered at 50N 145W), b) the eastern equatorial Pacific (5S 91W), c) the site of the Southern Ocean Time Series (SOTS; 47S 140E) and d) a site just south of the SOTS site (SOTS-S; 53S 140E). The colors represent Martin curve b values of 0.3 (purple), 0.5 (orange) and 0.8 (green), respectively. The colored envelopes display the standard deviation of the relative efficiency values for the 9 grid locations centered at the site. Site locations are illustrated in Figure S1.

Geographic variations in OIF efficiency and durability will be driven by spatial differences in the vertical mixing and circulation processes, the depths of the euphotic zone and surface mixed layer, as well as the time scale for air-sea CO_2 flux equilibration. Four canonical HNLC sites where OIF CDR is possible were chosen for illustrative purposes: the northeast Pacific Ocean at Station P (StaP), the eastern equatorial Pacific Ocean (EqPac), the sub-Antarctic Zone at the Southern Ocean Time Series (SOTS) site, and a site 600 km south of the SOTS site (SOTS-S; Figure S1). Large differences in relative efficiency time courses are seen as a function of the assumed *b* value for these four sites (Figure 3). Geographic differences can also be assessed by focusing on one of the assumed *b* values. For the deeper penetrating case (*b*=0.3), values of relative efficiency at 10 years range from 40% at the SOTS site to 54% at SOTS-S, to ≥ 60% for the equatorial and North Pacific sites (Figure 3). Similar differences are found among the four sites for the less penetrating Martin *b* values. Values of the efficiency at 100 years, $\varepsilon(100,\boldsymbol{x},b)$, show the expected strong dependence on the assumed *b* value with similar differences among the sites, although the difference among the sites is considerably muted (<10% for all cases) compared to the shorter timescales.

Differences among the $\varepsilon(t,\boldsymbol{x},b)$ values for the four sites arise due to local vertical mixing, air-sea CO_2 exchange and regional circulation processes. These processes determine the efficiency time course in two phases: an ingassing phase as atmospheric CO_2 slowly invades the surface ocean and a degassing phase as the remineralized DIC returns to the sea surface (Figure 1). The duration of the ingassing phase ranges from about 2 years (Station P) to 20 years (EqPac). During this phase the relative efficiency of the OIF perturbation reflects the net balance between the subduction of surface water parcels, which mixes the CO_2 deficit with the ocean interior, and the slow rate of air-sea CO_2 exchange. The highest $\varepsilon(20,\boldsymbol{x},b)$ values are found for the EqPac site, where mixed layer depths are considerably shallower than euphotic zone depths (Z_{ml} - Z_{eu} = -32 m vs. mean for the OIF region = 36 m) and time scales for air-sea CO_2 gas exchange are moderate (T_{CO2} = 178 days vs. OIF regional mean = 279 days). The lowest values of $\varepsilon(20,\boldsymbol{x},0.3)$ occur at the two Southern Ocean sites (41 & 52%) and this reflects the rapid mixing of the initial DIC perturbation below the surface, as mixed layer depths are deeper than the euphotic zone depths (Z_{ml} - Z_{eu} = 51 and 42 m for the SOTS and SOTS-S sites, respectively) which is deeper than the Z_{ml} - Z_{eu} OIF region mean (36 m). This mixing dilutes the OIF-induced DIC deficit that is in contact with the atmosphere and is also reflected in the very short mixed layer residence times of the Southern Ocean sites (< 5 days).

The declining efficiency phase is prolonged, due to the slow return timescales of deeply remineralized CO_2 back to the surface (Siegel et al., 2021). Here we focus on the efficiency at the 100-year time horizon as a metric of durability. Determinations of the durability index, $DI(\boldsymbol{x},b)$, for the four sites illustrate the expected dependence on the assumed b value, but also show differences among the sites. For example, the highest durability index values are found for the SOTS site where values are 99, 83 and 64% for b values of 0.3, 0.5 and 0.8, respectively. The lowest durability index values are found for the EqPac site where $DI(\boldsymbol{x},b)$ values are 77, 55 and 50% for three b values used. Interestingly, differences in the $DI(\boldsymbol{x},b)$ values among the sites do not consistently reflect differences in the return time scale for the remineralized DIC, $T_{ret}(\boldsymbol{x},b)$, as values of $T_{ret}(\boldsymbol{x},b)$ are all similar except the SOTS-S site (T_{ret}(SOTS-S,b) is approximately 20 years longer than the other three). Further, there appears to be an inverse relationship between $DI(\boldsymbol{x},b)$ and $\varepsilon(20,\boldsymbol{x},b)$ where the higher values of $DI(\boldsymbol{x},b)$ are found for the sites with lower $\varepsilon(20,\boldsymbol{x},b)$ and vice versa.

The spatial distribution in the relative efficiencies after 20, 100 and 500 years after an OIF CDR intervention occurs are shown for the intermediate b case (b = 0.5) in Figure 4. After 20 years, large spatial differences in relative efficiencies range from ~10% to more than 70%. Low relative efficiencies ($\varepsilon(20,\boldsymbol{x},0.5)$ < 30%) are found in shallow seas and near coasts where sinking particles cannot penetrate to great depths. Low $\varepsilon(20,\boldsymbol{x},0.5)$ values are also found in the Southern Ocean in the polar frontal zone, where

the initial mixing of the OIF CDR perturbation and the subduction of surface water parcels to depth occurs faster than the atmosphere can equilibrate to the initial negative surface DIC perturbation (Yamamoto et al. 2024; Zhou et al. 2025).

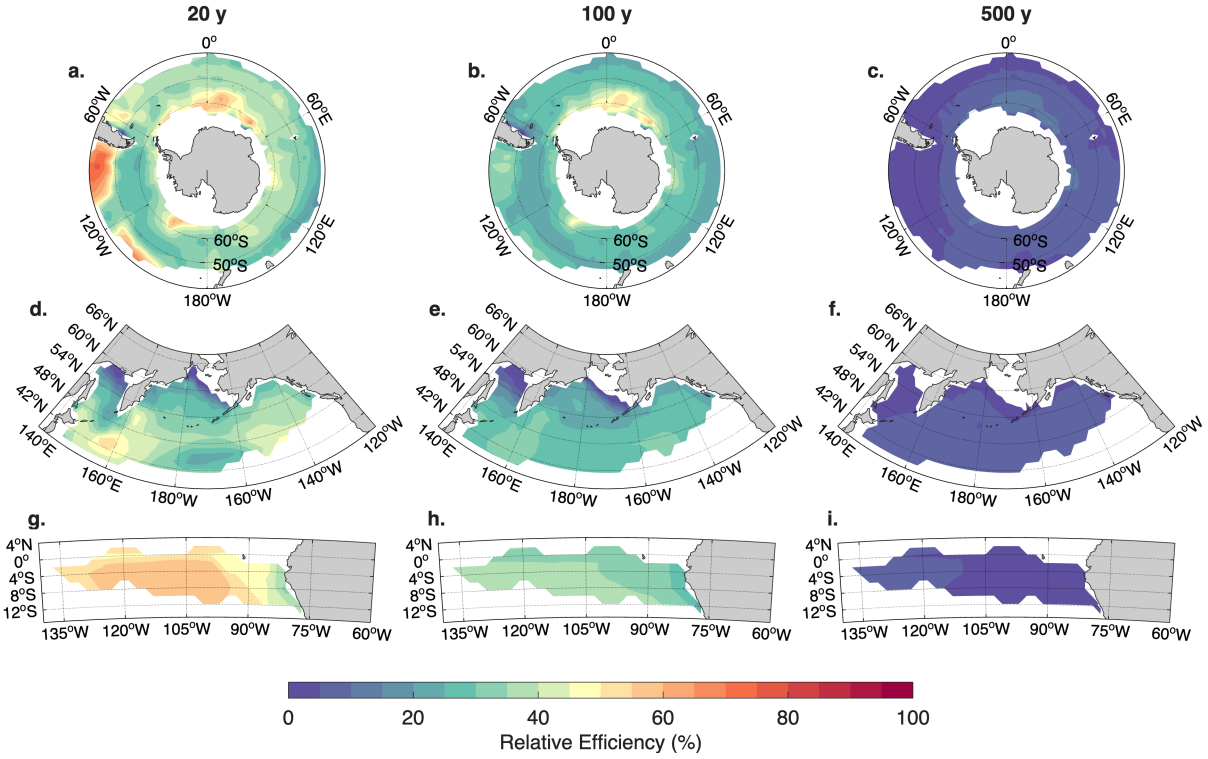


Figure 4. Relative efficiency values at 20, 100 and 500 years after the OIF CDR intervention for a Martin *b* value of 0.5 for sites for the (top row) Southern Ocean, (middle) North Pacific, and (bottom) Eastern Equatorial Pacific. Same plots for Martin *b* values of 0.3 and 0.8 are shown in Figures S9 and S10, respectively.

After 100 years, values of $\varepsilon(100,\boldsymbol{x},0.5)$ are reduced, as expected, and the global mean value decreases to 27% (stdev. = 8%). The spatial patterns are also muted ranging from roughly 20 to 35%. However, there are notable exceptions, particularly in the Southern Ocean south of the Antarctic Front at ~20°E, where values of $\varepsilon(100,\boldsymbol{x},0.5)$ remain greater than 40% (Figure 4b). This supports the assertion that this region could be a suitable site to conduct OIF CDR (Bach et al. 2023b). After 500 years, values of $\varepsilon(500,\boldsymbol{x},0.5)$ are further reduced as the CDR DIC perturbation returns to the atmosphere (Figures 4c, f & i). However, the spatial patterns in $\varepsilon(500,\boldsymbol{x},0.5)$ largely remain the same as those found after 100 years.

The importance of the remineralization length scale, the assumed *b* value, on the spatial distribution of relative efficiencies after 100 years is shown in Figure 5 for the three different b values explored here. As expected, dramatic differences in the overall values of $\varepsilon(100,\boldsymbol{x},b)$ are found. Global mean values of $\varepsilon(100,\boldsymbol{x},b)$ range from 42% (stdev. = 10%) for the b=0.3 case to 16% (stdev. = 6%) for the b=0.8 case. The spatial patterns are very similar to b=0.5 case shown previously, although the amplitude of the

differences is greater for the small *b* case and more muted for the larger *b* case. In particular, the spatial distribution of the deeply penetrating (b=0.3) case shows broad regions in the global ocean where values of $\varepsilon(100,\boldsymbol{x},0.3)$ are greater than 50% (Figure 5a, d and g), illustrating that OIF CDR in these regions could lead to durable CDR if organic carbon is exported deeply into the interior.

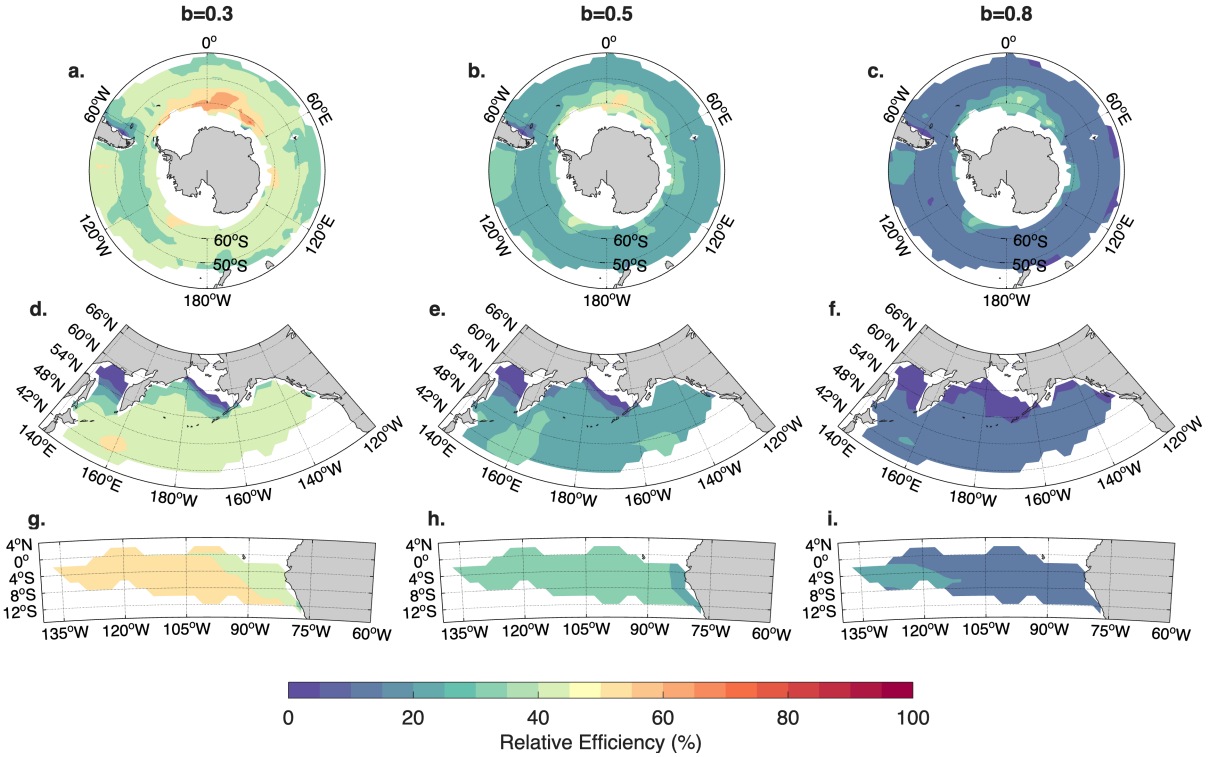


Figure 5. Relative efficiency values at 100 years after the OIF CDR intervention occurred shown for sites in the Southern Ocean, North Pacific, and Eastern Equatorial Pacific for the three Martin parameters explored (b = 0.3, 0.5 & 0.8). Only regions where annual mean surface NO_3 concentrations exceed 5μM and < 50% ice cover are shown.

Spatial variations in the centennial scale durability index (Eq. 3) show regions of near complete durability (nearly 100%), while in others durability values are much smaller, in places lower than 50% (Figure 6). Regions with the lowest $DI(\boldsymbol{x},b)$ values are associated with shallow seas or regions where large-scale vertical circulations are found (equatorial upwelling, boundaries of subtropical gyres, etc.). Among the three basins where HNLC conditions are found, values of $DI(\boldsymbol{x},b)$ are largest in the Southern Ocean and smallest in the eastern equatorial Pacific. As expected, the durability decreases with shallower particle penetration (higher b value), but this dependence is strongest in the equatorial Pacific and weakest in the Southern Ocean.

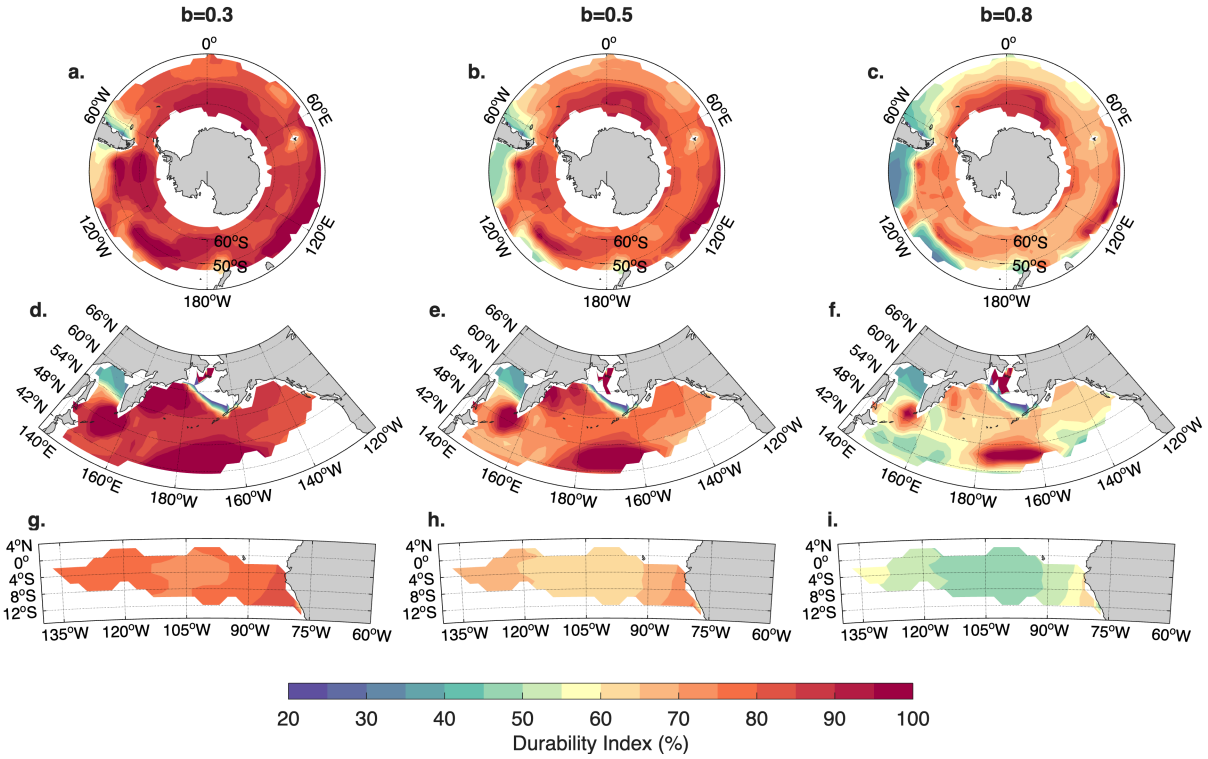


Figure 6. Durability index distributions, $DI(\boldsymbol{x},b)$, for HNLC regions in the Southern Ocean, North Pacific, and Eastern Equatorial Pacific for the three Martin parameters explored (b = 0.3, 0.5 & 0.8).

4. Discussion

The results presented show that OIF perturbations to the dissolved inorganic carbon concentration distribution are an inefficient CDR strategy compared with direct air capture CDR. However, a large fraction of the OIF sequestered carbon will remain isolated from the atmosphere for more than 100 years. The depth scale which the OIF perturbation penetrates beneath the euphotic zone, parameterized using a power law function with depth and an assumed b value (Equation 3), has first order controls on both the efficiency and durability of OIF CDR. The processes of air-sea CO_2 exchange, subduction of surface water parcels, and mixing of the CDR-induced DIC perturbation are also important, combining to create the spatial variations in OIF CDR efficiency. Last, OIF CDR is not permanent, and the temporarily sequestered atmospheric CO_2 will eventually return to the sea surface where it is exchanged back to the atmosphere. In the following, we address where OIF is most efficient and durable, discuss some of the strengths and limitations of the present modeling study, and conclude assessing the potential and some of the challenges of OIF as an effective CDR strategy.

4.1 Where is OIF CDR Most Efficient and Durable and Why?

Understanding where and under what conditions is OIF CDR most efficient and durable would be useful for planning at-scale implementation. To address this issue, we map out the regions of the ocean where the upper 25th percentile of $\varepsilon(20, \boldsymbol{x}, b)$ and $DI(\boldsymbol{x},b)$ values are found. Figure 7 illustrates the locations for the b = 0.5 case for high efficiencies (orange-red) and durability (violet). Results from the other two b value case are similar and are shown in the supplemental materials (Figures S11 & S12). The highest OIF efficiencies (red & orange in Figure 7) are found throughout the equatorial Pacific and portions of the subtropical oceans, while regions where the highest durability indices (violet & orange) are found largely in the Southern Ocean, particularly south of the Antarctic Front. For the most part, there is a lack of correspondence of regions where OIF CDR is both efficient and durable, suggesting that the processes creating efficient OIF incorporation of atmospheric CO_2 have little to do with those maximizing the durability of the sequestered CO_2 and vice versa. That said, there is one region in the Atlantic and Indian Ocean sectors of the Sothern Ocean south of the Antarctic Front that is both efficient and durable (orange in Figure 7). For the b = 0.5 case, this region of overlap is small and corresponds to about 6% of the total number of grid locations where OIF possible.

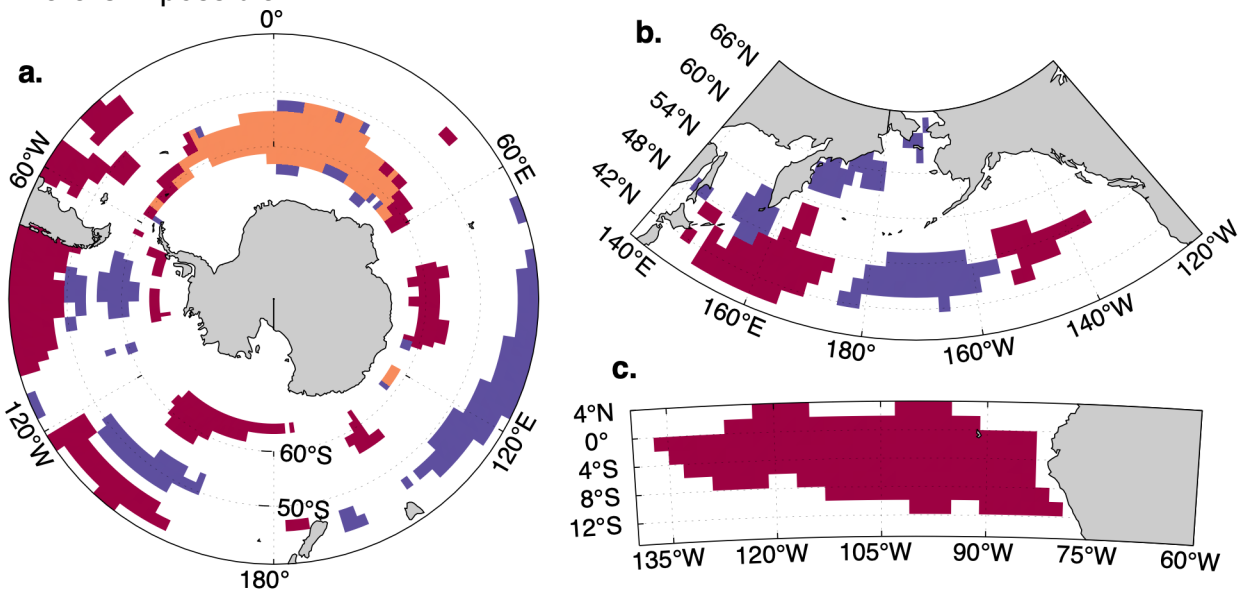


Figure 7. Locations where the best OIF CDR efficiency and durability are found for the b = 0.5 case. Shown are locations where the best 25% of the $\varepsilon(20, \boldsymbol{x}, 0.5)$ (red) and $DI(\boldsymbol{x},0.5)$ (violet) are found. The orange regions show where the highest 25% OIF efficiency and durability metrics coincide. Similar depictions for the b = 0.3 and the b = 0.8 cases are given in the supplemental figures (see Figures S11 & S12).

The assessment of mean values for relevant time and depth scales for locations where OIF is both most and least efficient and durable can then be used to diagnose potential drivers for these patterns. Table 1 provides conditional averaged values of the time

scales of air-sea CO_2 flux equilibration, $T_{CO2}(x)$, the subduction of surface water parcels, $T_{sub}(x)$, return time of the remineralized DIC, $T_{remin}(x,b)$, as well as difference between the mixed layer depth and the euphotic zone depth, $Z_{ml}(x)$-$Z_{eu}(x)$. Mean values for the metrics are calculated for the upper quadrille for the $\varepsilon(20,\boldsymbol{x})$ and $DI(\mathbf{x})$ distributions ("best"), the lower quadrille ("worst") and where the "best" locations for efficiency and durability coincide ("both").

The conditionally averaged time and depth metrics for the best and worst sites clearly illustrate their importance on setting OIF efficiencies. The most efficient locations are characterized by shorter time scales for air-sea flux equilibration, $T_{CO2}(\boldsymbol{x})$, longer residence times for water parcels to remain in the mixed layer, $T_{sub}(\boldsymbol{x})$, longer return times for remineralized DIC to return to the sea surface, $T_{remin}(\boldsymbol{x})$, as well as small differences between $Z_{ml}(\boldsymbol{x})$ and $Z_{eu}(\boldsymbol{x})$ (Table 1). This is expected as shorter flux equilibration time scales and longer surface water parcel residence and remineralized DIC retention times should lead to faster atmospheric CO_2 incorporation and thereby better OIF efficiencies. The worst efficiencies are found in regions associated with long flux equilibration time, short surface residence and remineralization return times and considerably deeper mixed layer depths than euphotic zone depths. If Z_{ml} is deeper than Z_{eu}, the OIF-induced DIC perturbation will mix throughout the deeper mixed layer, which includes the remineralized OIF biomass. This will reduce the DIC deficit in contact with the atmosphere and its potential to sequester atmospheric CO_2. It is interesting to note that values of $T_{CO2}(\boldsymbol{x})$ for both the best and worst regions are greater than the OIF domain mean suggesting that air-sea CO_2 flux processes may only have a limited impact on controlling OIF efficiency.

Table 1: Conditionally averaged mean values for important time and depth scale metrics. Shown are mean values for the entire region where OIF is possible ("total"), regions where the upper ("best") and lower ("worst") quadrilles for the $\varepsilon(20,\boldsymbol{x})$ and $DI(\mathbf{x})$ values are found. Also shown are mean metrics for the intersection of the upper quadrilles for the $\varepsilon(20,\boldsymbol{x})$ and $DI(\mathbf{x})$ values. Shown is the b = 0.5 case and similar statistics for the other cases may be found in Table S1.

Metrics for b=0.5	T_{CO2} (d)	T_{sub} (d)	T_{remin} (y)	Z_{ml}-Z_{eu} (m)
Total OIF Region	218.7	84.4	63.3	35.9
Best ε(x,20)	275.1	106.3	82.5	7.8
Worst ε(x,20)	369.0	63.8	61.0	60.9
Best *DI*(x)	362.1	89.0	79.9	50.6
Worst *DI*(x)	244.7	68.4	55.7	7.5
Best ε(x,20) & *DI*(x)	380.5	169.7	102.3	29.6

Locations with the highest durability metrics are associated with relatively deeper mixed layer depths and long surface residence and remineralization return time scales. If Z_{ml} is considerably deeper than Z_{eu}, OIF efficiencies will be lower as shown previously, but the atmospheric CO_2 that is incorporated into DIC will mix throughout a deeper mixed layer, further into the ocean interior, which will enable it to be sequestered from the atmosphere for longer. Conversely, locations with the lowest durability indices are characterized by small differences between $Z_{ml}(\boldsymbol{x})$ and $Z_{eu}(\boldsymbol{x})$ and smaller values for the subduction and remineralization return time scales. Again, the time scales for air-sea flux equilibration, $T_{CO2}(\boldsymbol{x})$, for both the best and worst durability regions are longer than the OIF domain mean, illustrating that this metric is not important for setting the durability.

Interestingly, the sites where both the best OIF efficiency and durability metrics are found can be characterized by moderate differences between $Z_{ml}(\boldsymbol{x})$ and $Z_{eu}(\boldsymbol{x})$, but substantially larger values for the subduction and remineralization return time scales than are found in any of the other cases (Table 1).

We can summarize these results by comparing the time scale and depth metrics for the best cases for both efficiency and durability. First, we find that values of OIF efficiency are much higher and durability metrics are lower when the depths for $Z_{ml}(\boldsymbol{x})$ and $Z_{eu}(\boldsymbol{x})$ are similar, whereas the efficiency metrics are lower and durability indices greater when $Z_{ml}(\boldsymbol{x})$ is much deeper than $Z_{eu}(\boldsymbol{x})$. When $Z_{ml}(\boldsymbol{x})$ is substantially deeper than $Z_{eu}(\boldsymbol{x})$, the OIF DIC perturbation is both diluted and homogenized shortly after deployment reducing efficiency levels. Further, the small amount of atmospheric CO_2 that is sequestered is mixed deeper into the water column and will be more durably stored. When the $Z_{ml}(\boldsymbol{x})$ and $Z_{eu}(\boldsymbol{x})$ depths are similar, this mixing of the initial DIC perturbation and sequestered CO_2 does not occur and efficiencies are higher while durability metrics are lower. Together, this points to the importance of vertical mixing processes on setting OIF efficiency and durability levels.

Second, we find that the values for both $T_{sub}(\boldsymbol{x})$ and $T_{remin}(\boldsymbol{x},b)$ are larger for the best cases for both efficiency and durability than they are for the worst cases for both metrics. This suggests that both mixed layer water parcel residence times and the time scales of return set both the levels of OIF efficiency and durability. For sites where both the best OIF efficiency and durability metrics are found, the very large values for both $T_{sub}(\boldsymbol{x})$ and $T_{remin}(\boldsymbol{x},b)$ appear to outweigh the moderate differences between $Z_{ml}(\boldsymbol{x})$ and $Z_{eu}(\boldsymbol{x})$ (Table 1). Again, values of $T_{CO2}(\boldsymbol{x})$ for the region where both best cases are found also higher than mean values found for the entire OIF domain, indicating the lesser importance of CO_2 gas exchange time scales compared with the other metrics.

Together, this analysis illustrates the importance of the physical processes of vertical mixing and the residence time of surface water parcels on setting the efficiency and

durability of OIF CDR. This will be significant during the early stages after an OIF deployment as the surface water parcels are mixed and subducted as the OIF DIC perturbation is formed. Last, this analysis was conducted holding the characteristics of the OIF remineralization profile, the value of Martin's *b*, constant. Results presented already have illustrated the critical role that specification of the OIF remineralization profile has on OIF efficiencies and to a somewhat lesser degree on OIF durability metrics (Figure 2).

4.2 Assumptions and Caveats

There are many assumptions in our assessment of the efficiency and durability of ocean iron fertilization as an atmospheric CO_2 removal strategy. To start, the experimental design is highly idealized. We simply assume that OIF CDR will remove a finite amount of DIC from the euphotic zone and that this biomass is instantaneously remineralized and redistributed within the water column and at the seafloor. The impacts of the OIF redistributed carbon on atmospheric CO_2 concentrations is then assessed as a function of time from months to 1000 years. There are, of course, a suite of ecological and biogeochemical processes that govern the interactions among an iron addition, ocean ecosystems and atmospheric CO_2 concentrations that are not considered. Thus, our study does not address how OIF CDR would or could be conducted operationally, or whether (or even if) additional carbon export would be stimulated via OIF. Rather we focus on the physical and chemical principles that regulate OIF efficiency and durability assuming that an OIF-induced perturbation of the vertical DIC profile can be created at that site.

The modeling system is based upon the OCIM transport operator (DeVries and Primeau, 2011; Holzer et al., 2021), which represents the mixing and circulation of a steady-state contemporary ocean. Hence, the effects of intraseasonal, seasonal or interannual changes are not considered. Further, changes in the air-sea forcings or carbonate system parameters are not considered as well. However, the framework of the present modeling system has been used to successfully model many important ocean biogeochemistry problems including the biological carbon pump (Nowicki et al. 2022), the oceanic fates of anthropogenic CO_2 emissions (DeVries, 2014; DeVries et al. 2023) and the efficiency and durability dynamics of ocean alkalinity enhancement CDR (Yamamoto et al. 2022) and seaweed cultivation and purposeful sequestration CDR (Sten et al. 2026). Hence, the OCIM frame employed here should be appropriate for this application.

The results presented also illustrate the importance of the vertical profile of the perturbed DIC profile due to the OIF perturbation. There is no observational data to quantify the remineralization profile due to OIF CDR and its quantification remains an important unknown. The range of *b* values explored (0.3 to 0.8) correspond with the low

end of the range of values reported by Buesseler et al. (2020). Results found using the Martin curve's canonical value, b=0.8, shows that OIF CDR will be inefficient, with mean $\varepsilon(20,\boldsymbol{x},0.8)$ values that are four times lower than would be found for direct air capture (Figure 2). We include deeper penetrating remineralization b values (b=0.3) that likely occurs if an OIF action would create phytoplankton blooms with larger phytoplankton taxa (i.e., diatoms) that produce rapidly sinking POC fluxes (Smetacek et al. 2012; Buesseler et al. 2024). Work here shows that global mean values of $\varepsilon(20,\boldsymbol{x},0.3)$ are two-times that found using canonical b values (for $\varepsilon(20,\boldsymbol{x},0.8)$). This suggests that until field-verified OIF remineralization profile parameterizations are available, Earth system model assessments of OIF CDR performance and impacts (Tagliabue et al. 2023; Noh et al. 2025; Yu et al. 2026) should consider the full range of possibilities in their parameterizations of the OIF-induced DIC remineralization profile.

Finally, the model system used here only simulates the ocean DIC distribution and its interactions with the atmosphere via air-sea exchange that is created by an OIF intervention. The model does not consider many things, the creation of the OIF DIC perturbation, its effects on local or downstream nutrient availability, potential interactions between the perturbed DIC distribution and the base biological cycles nor interactions with other sources or sinks such as the terrestrial biosphere. This leaves many important questions about the efficacy and suitability of OIF CDR requiring detailed modeling and field studies to address.

4.3 Is Ocean Iron Fertilization a Viable CDR Strategy?

The present results illustrate several important issues that must be considered if OIF CDR is to be deployed at scale to help achieve global negative net CO_2 emission goals. The efficiency of OIF will be two to four times lower than that expected for direct air capture (Figure 2). The degree of inefficiency is strongly dependent upon how far the OIF-induced DIC redistribution penetrates into the ocean interior, how much of the upper layer DIC perturbation is homogenized and the time that surface water parcels remain in contact with the atmosphere. These limitations may be one reason why modern global Earth System Model (ESM) simulations of large scale OIF additions (Tagliabue et al. 2023; Noh et al. 2026; Yu et al. 2026) predict nearly a 10-fold lower drawdown of atmospheric CO_2 levels compared with pioneering OIF box model analyses (Peng and Broecker, 1991; Joos et al. 1991), which assume that all of the available excess nitrogen would be biologically utilized resulting in the complete incorporation of atmospheric CO_2. Here, only a fraction of the CO_2 uptake potential is available, as much of the upper ocean OIF DIC perturbation has been either mixed out vertically or subducted from the sea surface before air-sea CO_2 exchanges have completed.

The OIF-induced DIC redistribution profile has a critical role in setting the initial relative efficiency levels, determining durability and thereby, for performing accurate carbon accounting. However, its quantification from field measurements will be a difficult task as assessments of sinking particle flux attenuation profiles remains uncertain (Cael and Bisson, 2018; Buesseler et al. 2020; Taylor et al. 2026). The determination of the OIF-induced DIC redistribution profile will be the difference between those measured for an OIF CDR deployment and a baseline without the CDR action. The construction of this profile will combine the profile of the DIC drawdown due to the OIF-created phytoplankton bloom and the differences in the remineralization profiles beneath the euphotic zone between the OIF site and the baseline. As the OIF-induced remineralization profile would be the difference in two rather poorly quantified fluxes, uncertainty levels in its determination will be amplified. Clearly, pilot-scale field observations are required to develop this predictive understanding (Buesseler et al. 2024). The importance of the penetration of OIF biomass into the interior also raises the question whether OIF-induced blooms could be "engineered" to optimize OIF CDR performance by altering the procedures or materials used to stimulate the OIF bloom.

There are many other issues that were not addressed here, but must be considered if OIF is to be considered a viable CDR strategy. These include the local and remote impacts of OIF nutrient utilization, the ability of OIF to scale to gigatons CO_2 per year globally, the environmental impacts that it will create, both intended and unintended, and whether the assumed perturbation to the DIC distribution due to OIF could actually be achieved (NASEM, 2022; Buesseler et al. 2024). Beyond these biogeochemical and ecological concerns, there are a host of other equally important issues that also must be considered (NASEM, 2026; Doney et al. 2024). These include assessments of the costs of required infrastructure to achieve Gt CO_2 per year scalings, adoption of the required monitoring, reporting and verification methodologies as well as proper governance structures, all while maintaining societal acceptability and justice for all affected parties (Cooley et al. 2023; Doney et al. 2024; Oschlies et al. 2025; NASEM, 2026).

This brings us back to the question stated in this section's title; *Is Ocean iron fertilization a viable CDR strategy*? Our goal here is to assess the efficiency and durability of OIF CDR and to understand the processes controlling its variations in space and time. However, as discussed above, simply quantifying the OIF efficiency and durability is not all that needed to answer this question. In the best of worlds, the costs and benefits of conducting OIF CDR at scale would be weighed against the cost and benefits of other CDR approaches, and against a no-action policy. The present results provide some of the pieces needed for that calculation and present both hopes and challenges facing OIF CDR as a potential net negative emission solution.

Acknowledgements:

The authors would like to thank Ken Buesseler for comments on an earlier draft of this manuscript and our many colleagues for useful conversations about marine CDR. DAS acknowledges initial support on this work from the Advanced Research Projects Agency-Energy (ARPA-E) Open 21 Award (DE AR0001559). TD acknowledges support from the U.S. National Science Foundation through award 2049509. Kaley Sten created the conceptual figure using BioRender (https://biorender.com).

Conflicts of Interest

The authors declare no conflicts of interest relevant to this study.

Availability Statement

The OIF efficiency and durability data and model codes are available on the FigShare database (Siegel, 2026). The OCIM2-48L transport model is publicly available on the FigShare database (DeVries, 2022).

References:

Bach, L.T., Ho, D.T., Boyd, P.W. and Tyka, M.D., 2023a. Toward a consensus framework to evaluate air–sea CO_2 equilibration for marine CO_2 removal. *Limnol. Oceanogr. Letters*, **8**, 685-691. https://doi.org/10.1002/lol2.10330.

Bach, L.T., Tamsitt, V., Baldry, K., McGee, J., Laurenceau-Cornec, E.C., Strzepek, R.F., and others, 2023. Identifying the most (cost-) efficient regions for CO_2 removal with iron fertilization in the Southern Ocean. *Glob. Biogeochem. Cyc.,* **37**(11), e2023GB007754. https://doi.org/10.1029/2023GB007754.

Boyd, P. W., Jickells, T., Law, C.S., Blain, S., Boyle, E.A., Buesseler, K.O., and others 2007, Mesoscale iron enrichment experiments 1993-2005: synthesis and future directions. *Science* **315**, 612–617. https://doi.org/10.1126/science.1131669.

Buesseler, K.O., Boyd, P.W., Black, E.E., & Siegel, D.A., 2020, Metrics that matter for assessing the ocean biological carbon pump. *Proceedings of the National Academy of Sciences*, *117*(18), 9679-9687, https://doi.org/10.1073/pnas.1918114117.

Buesseler, K., D. Bianchi, F. Chai, J.T. Cullen, M. Estapa, N. Hawco, and others, 2024, Next steps for assessing ocean iron fertilization for marine carbon dioxide removal. *Frontiers in Climate*, **6**,1430957. https://doi.org/10.3389/fclim.2024.1430957.

Cael, B. B., & Bisson, K. 2018. Particle flux parameterizations: Quantitative and mechanistic similarities and differences. *Frontiers in Marine Science*, **5**, 395. https://doi.org/10.3389/fmars.2018.00395.

Cooley, S.R., Klinsky, S., Morrow, D.R. and Satterfield, T., 2023. Sociotechnical considerations about ocean carbon dioxide removal. *Annual Review of Marine Science*, **15**, 41-66. https://doi.org/10.1146/annurev-marine-032122-113850.

633 DeVries T., 2014, The oceanic anthropogenic CO_2 sink: Storage, air-sea fluxes, and
634 transports over the industrial era *Glob. Biogeochem. Cyc.,* **28**, 631-647.
635 https://doi.org/10.1002/2013GB004739.

636 DeVries, T., 2022, OCIM2-48L abiotic ocean carbon cycle model output. figshare.
637 Dataset. https://doi.org/10.6084/m9.figshare.19341974.v2.

638 DeVries T., and F. Primeau, 2011, Dynamically and observationally constrained
639 estimates of water-mass distributions and ages in the global ocean. *J. Phys.*
640 *Oceanogr.* **41** 2381–2401. https://doi.org/10.1175/JPO-D-10-05011.1.

641 DeVries, T., Yamamoto, K., Wanninkhof, R., Gruber, N., Hauck, J., Müller, J. D., et al.,
642 2023, Magnitude, trends, and variability of the global ocean carbon sink from 1985 to
643 2018. *Global Biogeochemical Cycles*, 37, e2023GB007780.
644 https://doi.org/10.1029/2023GB007780

645 Doney S.C., Wolfe W.H., McKee D.C. and Fuhrman J.G., 2024, The science,
646 engineering, and validation of marine carbon dioxide removal and storage. *Annual*
647 *Review of Marine Science*, https://doi.org/10.1146/annurev-marine-040523-014702.

648 Edwards, M. R., Geden, O., Gidden, M. J., Lamb, W. F., Minx, J. C., Nemet, and others
649 (eds.), 2026, *The State of Carbon Dioxide Removal 3rd Edition*.
650 https://doi.org/10.17605/OSF.IO/ZRD65.

651 GESAMP, 2019, High level review of a wide range of proposed marine geoengineering
652 techniques. (Boyd, P.W. and Vivian, C.M.G., eds.). (IMO/FAO/UNESCO-
653 IOC/UNIDO/WMO/IAEA/UN/UN Environment/ UNDP/ISA Joint Group of Experts on
654 the Scientific Aspects of Marine Environmental Protection).
655 Rep. Stud. GESAMP No. 98, 144 p.

656 Holzer M., DeVries, T. and de Lavergne, C., 2021, Diffusion controls the ventilation of a
657 Pacific shadow zone above abyssal overturning. *Nat. Commun.,* **12,** 4348.
658 https://doi.org/10.1038/s41467-021-24648-x.

659 Jickells, T.D., An, Z.S., Andersen, K.K., Baker, A.R., Bergametti, G., Brooks, N., and
660 others, 2005. Global iron connections between desert dust, ocean biogeochemistry,
661 and climate. *Science*, **308**, 5718, 67-71. https://doi.org/10.1126/science.1105959.

662 Joos F., J. Sarmiento, U. Siegenthaler, 1991, Estimates of the effect of Southern Ocean
663 iron fertilization on atmospheric CO2 concentrations. *Nature,* **349**, 772–775.
664 https://doi.org/10.1038/349772a0,

665 Martin, J.H., Knauer, G.A.; Karl, D.M.; Broenkow, W.W.,1987. VERTEX: Carbon cycling
666 in the northeast Pacific. *Deep Sea Research Part A,* **34** (2): 267–285.
667 doi:10.1016/0198-0149(87)90086-0.

668 Martin, J. H., 1990, Glacial-interglacial CO_2 change: the iron hypothesis.
669 *Paleoceanography* **5**, 1–13. https://doi.org/10.1029/PA005i001p00001.

670 National Academies of Sciences, Engineering, and Medicine (NASEM). 2019. *Negative*
671 *Emissions Technologies and Reliable Sequestration: A Research Agenda*.
672 Washington, DC: The National Academies Press.

https://www.nationalacademies.org/projects/DELS-BASCPR-16-01/publication/25259.

National Academies of Sciences, Engineering, and Medicine (NASEM). 2022. *A Research Strategy for Ocean-based Carbon Dioxide Removal and Sequestration*. Washington, DC: The National Academies Press. https://www.nationalacademies.org/projects/DELS-OSB-20-02/publication/26278.

National Academies of Sciences, Engineering, and Medicine (NASEM). 2026. *A Research Strategy for Ocean-based Carbon Dioxide Removal and Sequestration*. Washington, DC: The National Academies Press. https://doi.org/10.17226/29342.

Noh, K.M., Liu, X., Stock, C., McGillicuddy Jr, D. and Dunne, J., 2025. Revisiting the additionality and durability of carbon uptake in large-scale ocean iron fertilization. Preprint available at https://doi.org/10.21203/rs.3.rs-7717531/v1.

Nowicki, M., DeVries, T., & Siegel, D.A. 2022, Quantifying the carbon export and sequestration pathways of the ocean's biological carbon pump. *Global Biogeochemical Cycles*, 36, e2021GB007083. https://doi.org/10.1029/2021GB007083.

Oschlies, A., Bach L.T., Fennel K., Gattuso J.-P. and Mengis N., 2025, Perspectives and challenges of marine carbon dioxide removal. *Front. Clim*. 6, 1506181. https://doi.org/10.3389/fclim.2024.1506181.

Peng, T.H., and W.S. Broecker, 1991, Dynamic limitations on the Antarctic iron fertilization strategy. *Nature*, **349**, 227–229. https://doi.org/10.1038/349227a0.

Primeau, F., 2005, Characterizing transport between the surface mixed layer and the ocean interior with a forward and adjoint global ocean transport model. *Journal of Physical Oceanography*, **35**, 545-564. https://doi.org/10.1175/JPO2699.1.

Siegel, D.A., T. DeVries, S.C. Doney and T. Bell, 2021, Assessing the sequestration time scales of some ocean-based carbon dioxide reduction strategies. *Environ. Res. Lett.*, https://doi.org/10.1088/1748-9326/ac0be0.

Siegel, D., 2026, Data and codes for "On the Efficiency and Durability of Ocean Iron Fertilization as a Carbon Dioxide Removal Solution" by Siegel, Yamamoto & DeVries. figshare. Dataset. https://doi.org/10.6084/m9.figshare.34328118.v1.

Smetacek, V., Klaas, C., Strass, V. *et al.*, 2012, Deep carbon export from a Southern Ocean iron-fertilized diatom bloom. *Nature* **487**, 313–319, https://doi.org/10.1038/nature11229.

Sten, M., K. Yamamoto, K., T. DeVries, S.J.E. Krause & D.A. Siegel, 2026. On the efficiency and durability of purposefully sinking seaweed biomass as a marine carbon dioxide removal strategy. *Earth's Future*, **14**, e2025EF007628. https://doi.org/10.1029/2025EF007628.

Tagliabue A., B.S. Twining, N. Barrier, O. Maury, M. Berger & L. Bopp, 2023. Ocean iron fertilization may amplify climate change pressures on marine animal biomass for limited climate benefit. *Global Change Biology,* **29**, 5250–5260, https://doi.org/10.1111/gcb.16854.

Taylor, K., Ferrari, R., & Cael, B.B., 2026. Modeling variability in vertical profiles of particulate organic carbon flux. *Geophysical Research Letters*, *53*, e2026GL121728. https://doi.org/10.1029/ 2026GL121728.

Yamamoto, K., T. DeVries and D.A. Siegel, 2024, Metrics for quantifying the efficiency of atmospheric CO_2 reduction by marine carbon dioxide removal (mCDR). *Environ. Res. Lett.* **19**, 104053**,** https://doi.org/10.1088/1748-9326/ad7477.

Yoon, J.-E., Yoo, K.-C., Macdonald, A. M., Yoon, H. I., Park, K. T., Yang, E. J., et al., 2018, Reviews and syntheses: ocean iron fertilization experiments – past, present, and future looking to a future Korean iron fertilization experiment in the Southern Ocean (KIFES) project. *Biogeosciences,* **15**, 5847–5889. https://doi.org/10.5194/bg-15-5847-2018.

Yu, J., Moore, J.K., Primeau, F.W., Michaels, A.F., Nuno, A.G., Krumhardt, K.M., *et al.* 2026, Climate benefit and ecological cost trade-offs for ocean iron fertilization. *Nature* **656**, 106–114. https://doi.org/10.1038/s41586-026-10795-y.

Zhou, M., Tyka, M.D., Ho, D.T. et al., 2025, Mapping the global variation in the efficiency of ocean alkalinity enhancement for carbon dioxide removal. *Nat. Clim. Chang.* **15**, 59–65, https://doi.org/10.1038/s41558-024-02179-9.

References for the Supplementary Materials:

Boyer T. P., García, H. E., Locarnini, R. A., Zweng, M. M., Mishonov, A. V., Reagan, J. R., Weathers, K. A., Baranova, O. K., Paver, C. R., Seidov, D., and Smolyar, I. V. 2018. World Ocean Atlas 2018. Temperature, Salinity, Phosphate, and Silicate. NOAA National Centers for Environmental Information. Dataset. https://www.ncei.noaa.gov/archive/accession/NCEI-WOA18. Accessed 2021.

Broecker W.S. and Peng T.-H. 1974 Gas exchange rates between air and sea. *Tellus* **26** 21–35, https://doi.org/10.1111/j.2153-3490.1974.tb01948.x.

Kanamitsu, M., Ebisuzaki, W., Woollen, J., Yang, S.-K., Hnilo, J. J., Fiorino, M., and Potter, G. L. 2002. NCEP-DOE AMIP-II reanalysis (R-2) Bull. Am. Meteorol. Soc. 83 1631–43.

Lauvset, S. K., Key, R. M., Olsen, A., van Heuven, S., Velo, A., Lin, X., Schirnick, C., Kozyr, A., Tanhua, T., Hoppema, M., Jutterström, S., Steinfeldt, R., Jeansson, E., Ishii, M., Pérez, F. F., Suzuki, T., and Watelet, S. 2016. A new global interior ocean mapped climatology: the 1°x1° GLODAP version 2. *Earth Syst. Sci. Data* 8 325–340 https://doi.org/10.5194/essd-8-325-2016.

Nowicki, M., T. DeVries & D.A. Siegel, (2024). The influence of air-sea CO_2 disequilibrium on carbon sequestration by the ocean's biological pump. *Global Biogeochem. Cycles*, **38**, e2023GB007880. https://doi.org/10.1029/2023GB007880.

Yamamoto, K., DeVries, T. and Siegel, D.A., (2025). Corrigendum: Metrics for quantifying the efficiency of atmospheric CO2 reduction by marine carbon dioxide removal (mCDR)(2024 Environ. Res. Lett. 19 104053). *Env. Res. Lett.*, *20*(8), p.089501. https://doi.org/10.1088/1748-9326/adea88.

https://www.nationalacademies.org/projects/DELS-BASCPR-16-01/publication/25259.

National Academies of Sciences, Engineering, and Medicine (NASEM). 2022. *A Research Strategy for Ocean-based Carbon Dioxide Removal and Sequestration*. Washington, DC: The National Academies Press. https://www.nationalacademies.org/projects/DELS-OSB-20-02/publication/26278.

National Academies of Sciences, Engineering, and Medicine (NASEM). 2026. *A Research Strategy for Ocean-based Carbon Dioxide Removal and Sequestration*. Washington, DC: The National Academies Press. https://doi.org/10.17226/29342.

Noh, K.M., Liu, X., Stock, C., McGillicuddy Jr, D. and Dunne, J., 2025. Revisiting the additionality and durability of carbon uptake in large-scale ocean iron fertilization. Preprint available at https://doi.org/10.21203/rs.3.rs-7717531/v1.

Nowicki, M., DeVries, T., & Siegel, D.A. 2022, Quantifying the carbon export and sequestration pathways of the ocean's biological carbon pump. *Global Biogeochemical Cycles*, 36, e2021GB007083. https://doi.org/10.1029/2021GB007083.

Oschlies, A., Bach L.T., Fennel K., Gattuso J.-P. and Mengis N., 2025, Perspectives and challenges of marine carbon dioxide removal. *Front. Clim*. 6, 1506181. https://doi.org/10.3389/fclim.2024.1506181.

Peng, T.H., and W.S. Broecker, 1991, Dynamic limitations on the Antarctic iron fertilization strategy. *Nature*, **349**, 227–229. https://doi.org/10.1038/349227a0.

Primeau, F., 2005, Characterizing transport between the surface mixed layer and the ocean interior with a forward and adjoint global ocean transport model. *Journal of Physical Oceanography*, **35**, 545-564. https://doi.org/10.1175/JPO2699.1.

Siegel, D.A., T. DeVries, S.C. Doney and T. Bell, 2021, Assessing the sequestration time scales of some ocean-based carbon dioxide reduction strategies. *Environ. Res. Lett.*, https://doi.org/10.1088/1748-9326/ac0be0.

Siegel, D., 2026, Data and codes for "On the Efficiency and Durability of Ocean Iron Fertilization as a Carbon Dioxide Removal Solution" by Siegel, Yamamoto & DeVries. figshare. Dataset. https://doi.org/10.6084/m9.figshare.34328118.v1.

Smetacek, V., Klaas, C., Strass, V. *et al.*, 2012, Deep carbon export from a Southern Ocean iron-fertilized diatom bloom. *Nature* **487**, 313–319, https://doi.org/10.1038/nature11229.

Sten, M., K. Yamamoto, K., T. DeVries, S.J.E. Krause & D.A. Siegel, 2026. On the efficiency and durability of purposefully sinking seaweed biomass as a marine carbon dioxide removal strategy. *Earth's Future*, **14**, e2025EF007628. https://doi.org/10.1029/2025EF007628.

Tagliabue A., B.S. Twining, N. Barrier, O. Maury, M. Berger & L. Bopp, 2023. Ocean iron fertilization may amplify climate change pressures on marine animal biomass for limited climate benefit. *Global Change Biology,* **29**, 5250–5260, https://doi.org/10.1111/gcb.16854.

Earth's Future

Supporting Information for

On the Efficiency and Durability of Ocean Iron Fertilization as a Carbon Dioxide Removal Solution

David A. Siegel[1,2], Kana Yamamoto[1], and Tim DeVries[1,2]

[1]Earth Research Institute, University of California, Santa Barbara

[2]Department of Geography, University of California, Santa Barbara

*Corresponding Author's E-mail: david.siegel@ucsb.edu

Contents of this file

Text S1
Figures S1 to S12
Tables S1

Introduction

The following includes the detailed derivation of the linearized tracer equations used to solve for the CDR perturbations as well as supplemental figures and a supplemental table.

Text S1 - Derivation of the linearized DIC perturbation evolution equation

Here, we present the linearized approximation for the tracer equations that govern the perturbations to the ocean and atmospheric carbon reservoirs due to carbon dioxide removal (CDR) following Yamamoto et al. (2024) and Yamamoto et al. (2025). A coupled ocean-atmosphere model is used to simulate the ocean and atmospheric carbon perturbation from CDR. We model the atmosphere as a single reservoir and track the time history of the time evolution of the partial fraction of CO_2 (xCO_2, ppm) coupled to the air-sea CO_2 exchange summed over the ice-free ocean. For the ocean, we use a data-assimilated, global ocean circulation inverse model (OCIM). The OCIM estimates the climatological mean state of the ocean circulation for the modern ocean and casts it as a matrix transport operator (DeVries 2014; DeVries and Primeau 2011). Here we use the latest version, OCIM2-48L, which has a 2° horizontal resolution and 48

depth levels (Holzer *et al* 2021). The atmosphere is represented by a single well-mixed reservoir that exchanges CO_2 with each surface ocean grid cell. The distribution of dissolved inorganic carbon in the ocean (DIC, μmol kg^{-1}) and CO_2 in the atmosphere (xCO_2, ppm) is coupled by the air-sea CO_2 exchange:

$$\frac{\partial \mathrm{DIC}}{\partial t} = \mathbf{T} \cdot \mathrm{DIC} - \frac{1}{\rho z_1} F_{sea-air} + J_{bio} \qquad (S1)$$

$$\frac{\partial x\mathrm{CO}_2}{\partial t} = \frac{1}{M_{air}} \int_A F_{sea-air} dA + J_{other} \qquad (S2)$$

where ***T*** is the OCIM2-48L transport operator (yr^{-1}), $F_{sea\text{-}air}$ is the sea-to-air CO_2 flux (μmol m^{-2} yr^{-1}), J_{bio} is the biological sources and sinks of DIC (μmol kg^{-1} yr^{-1}), J_{other} represents the combined fluxes from other sources such as the terrestrial biosphere and anthropogenic CO_2 emissions (ppm yr^{-1}), M_{air} is the moles of air in the atmosphere (1.7×10^{20} mol), and dA is the area of each model surface ocean grid cell (m^2). We assume that the contribution of CO_2 to M_{air} is negligible. $F_{sea\text{-}air}$ is proportional to the difference between the partial pressures of CO_2 in the ocean ($pCO_{2,ocn}$, μatm) and atmosphere ($pCO_{2,atm}$, μatm):

$$F_{sea-air} = \rho K_w K_0 (pCO_{2,ocn} - pCO_{2,atm})(1 - f_{ice}) \qquad (S3)$$

where ρ is the seawater density (1025 kg m^{-3}), $pCO_{2,atm}$ is directly proportional to xCO_2 (assuming a sea surface pressure of 1 atm), K_w is the piston velocity (m yr^{-1}), K_0 is the CO_2 solubility in seawater (mol kg^{-1} atm^{-1}), and f_{ice} is the ice-covered fraction. $F_{sea\text{-}air}$ is positive when there is a net flux of CO_2 into the atmosphere.

$F_{sea\text{-}air}$ is non-linear with respect to DIC, but can be approximated by linearizing the carbonate system about the modern ocean state such that the air-sea CO_2 equilibration timescale (τ_{CO2}) is:

$$\tau_{CO2} = \frac{z_1 \beta}{K_w R} \qquad (S4)$$

where z_1 is the depth of the top model grid layer (m), β is the equilibrium ratio of DIC to dissolved CO_2 in seawater and R is the Revelle factor (Broecker and Peng 1974, Nowicki *et al* 2024). The global distribution of τ_{CO2} is plotted in Figure S8. The ocean carbonate parameters (β, R, K_0) are solved using CO2SYS (van Heuven *et al* 2011) with inputs of DIC and total alkalinity from the GLODAPv2 mapped climatology (Lauvset *et al* 2016); and phosphate, silicate, sea surface temperature, and sea surface salinity taken from the World Ocean Atlas 2018 (Boyer *et al* 2018). Values of the 10-m wind speeds (U_{10}) and f_{ice} are from the NCEP/DOE Reanalysis II dataset (Kanamitsu et al 2002), while determinations of the piston velocity, K_w, are based on a quadratic relationship on U_{10} (Wanninkhof 2014).

The coupled ocean and atmosphere carbon system is given in equations S1 and S2 with DIC denoting the dissolved inorganic carbon concentration in the ocean (μmol kg^{-1}) and xCO_2 denoting the mole fraction of atmospheric CO_2 (ppm). CDR introduces a perturbation in this coupled ocean-atmosphere system:

$$\frac{\partial(DIC + \Delta DIC)}{\partial t} = \boldsymbol{T} \cdot (DIC + \Delta DIC) - \frac{1}{\rho z_1}(F_{sea-air} + \Delta F_{sea-air}) + (J_{bio} + \Delta J_{bio}) - \Delta J_{CDR,ocn} \quad (S5)$$

$$\frac{\partial(xCO_2 + \Delta xCO_2)}{\partial t} = \frac{1}{M_{air}} \int_A (F_{sea-air} + \Delta F_{sea-air}) dA + (J_{other} + \Delta J_{other}) - \Delta J_{CDR,atm} \quad (S6)$$

where Δ denotes the anomalous perturbations due to the CDR action. By subtracting equations S1 and S2 from equations S5 and S6, we get the tracer equations of the ocean and atmosphere carbon perturbations due to CDR:

$$\frac{\partial \Delta DIC}{\partial t} = \boldsymbol{T} \cdot \Delta DIC - \frac{1}{\rho z_1} \Delta F_{sea-air} + \Delta J_{bio} - \Delta J_{CDR,ocn} \quad (S7)$$

$$\frac{\partial \Delta xCO_2}{\partial t} = \frac{1}{M_{air}} \int_A \Delta F_{sea-air} dA + \Delta J_{other} - \Delta J_{CDR,atm} \quad (S8)$$

As we linearized the carbonate system about the modern ocean state, the anomalous CO_2 gas exchange is:

$$\frac{\Delta F_{sea-air}}{z_1} \cong \frac{1 - f_{ice}}{\tau_{CO2}} \left(\Delta DIC - \frac{K_o \beta}{R} P_{atm} \Delta xCO_2 \right) \quad (S9)$$

We substitute equation S9 into equations S7 and S8 and assume that J_{bio} and J_{other} are not affected by the CDR perturbation (i.e. $\Delta J_{bio} = \Delta J_{other} = 0$). This results in the linearized approximation for the carbon anomaly introduced by the CDR action, or

$$\frac{\partial \Delta DIC}{\partial t} = \boldsymbol{T} \cdot \Delta DIC - \frac{1 - f_{ice}}{\tau_{CO2}} \left(\Delta DIC - \frac{K_o \beta}{R} P_{atm} \Delta xCO_2 \right) - \Delta J_{CDR,ocn} \quad (S10)$$

$$\frac{\partial \Delta xCO_2}{\partial t} = \frac{z_1 \rho}{M_{air}} \int_A \frac{1 - f_{ice}}{\tau_{CO2}} \left(\Delta DIC - \frac{K_o \beta}{R} P_{atm} \Delta xCO_2 \right) dA - \Delta J_{CDR,atm} \quad (S11)$$

The linearized system of equations for the impact of the CDT action is solved forward in time using the backward Euler method and matrix inversion with a time-varying time-step out to 1000 years. The time-steps are daily for the first 90 days, monthly thereafter until Year 5, annual thereafter until Year 100, decadal thereafter until Year 500, and centennial thereafter until Year 1000. The CDR perturbation is applied to both the atmosphere and to the ocean profile at the OCIM grid location. To simulate direct air capture, 1 ppm CO_2 per year is removed from the atmosphere for the first month of the simulations. To model OIF CDR, 1 Tg DIC is removed from the euphotic zone during the first month and that amount of DIC is redistributed below the euphotic zone following equation 2b.

Time scales for the retention of the OIF induced DIC perturbation in the near-surface mixed layer, $T_{sub}(\boldsymbol{x})$ (Figure S6) are determined as the time it takes for the concentration of a scalar released within the mixed layer to decrease by 50% of its original concentration. The mean time that the remineralized DIC below the euphotic zone from the OIF perturbation remains out of contact with the surface ocean, $T_{ret}(\boldsymbol{x},b)$ (Figure S7) are determined as the mean first passage time of the remineralized DIC beneath the euphotic zone from the OIF CDR perturbation to reach the sea surface. Values of $T_{ret}(\boldsymbol{x},b)$ are a function of the assumed b value used and Last, the time scale for equilibration of air-sea CO_2 gas exchange, $T_{CO2}(\boldsymbol{x})$, are determined for the surface mixed layer (Figure S8) using equation S4 based upon local carbonate chemistry, mixed layer depths and wind speed.

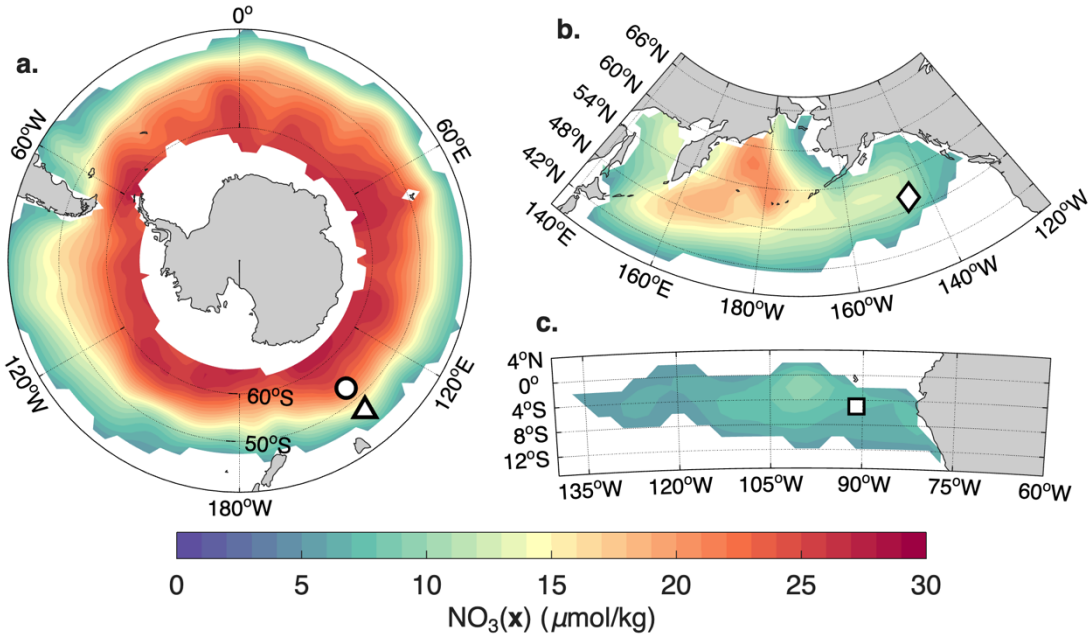


Figure S1: Nitrate nutrient concentrations (in μmol kg^{-1}) for a) Southern Ocean, b) North Subarctic Pacific Ocean and c) Equatorial Pacific Ocean. Solid black line shows 5 μmol/kg contour. Also shown are the sites shown in Figure 2 (circle = SOTS, triangle = South of SOTS, diamond = Station P, square = eastern equatorial Pacific station). Only data are shown for the domain where OIF is possible, which is defined here by surface nitrate concentrations greater than 5 μmol kg^{-1} and annual ice covers less than 50%.

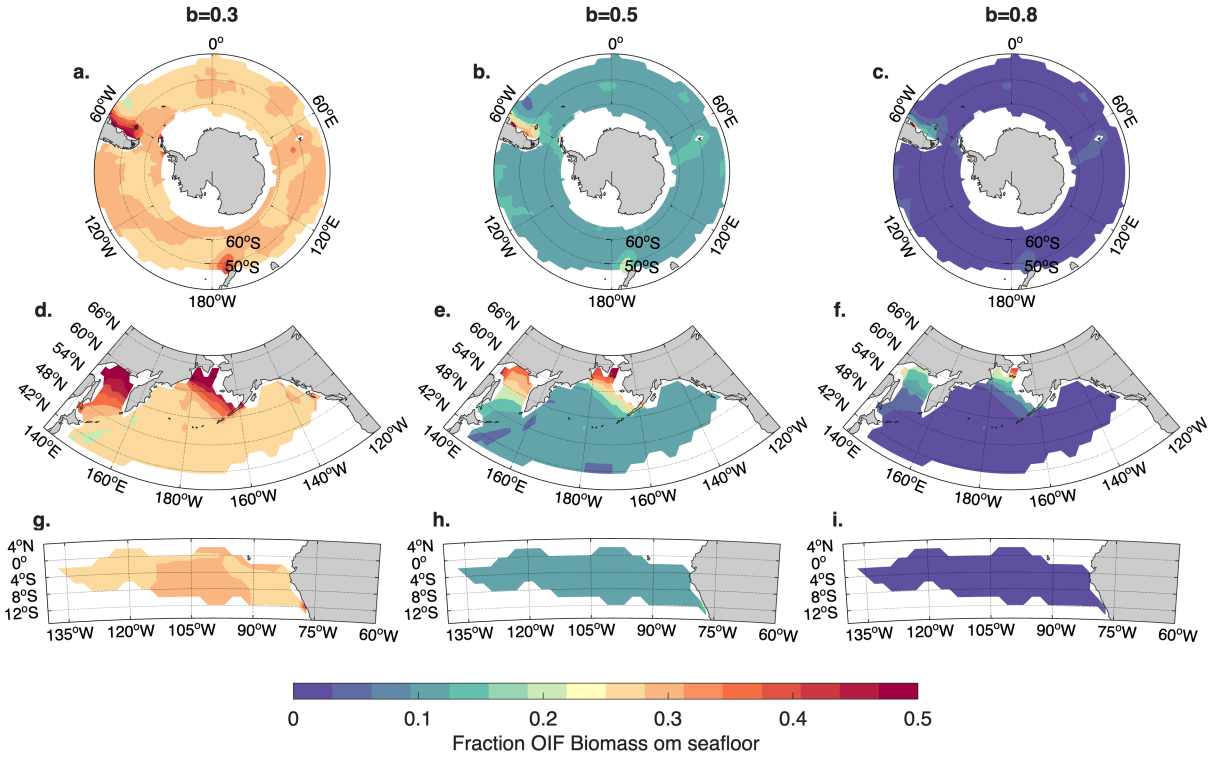


Figure S2: Spatial distribution of the fraction of the initial OIF perturbation that reaches the seafloor for three different export efficiencies for the OIF domain. Global mean values for the regions where OIF is possible are 0.31 (stdev. 0.05), 0.14 (0.04) and 0.05 (0.03) for *b* values of 0.3, 0.5 & 0.8, respectively.

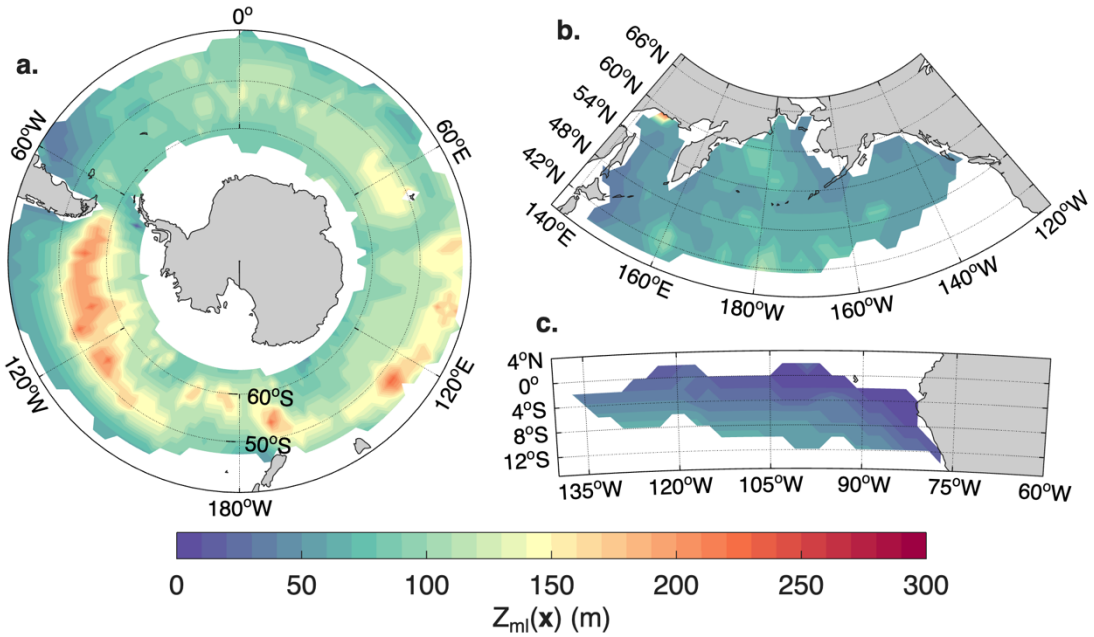


Figure S3: Spatial distribution of the annual mean mixed layer depth (m), $Z_{ml}(\boldsymbol{x})$, for the OIF domain. OIF regional mean $Z_{ml}(\boldsymbol{x})$ values are 96 m (38 m stdev.).

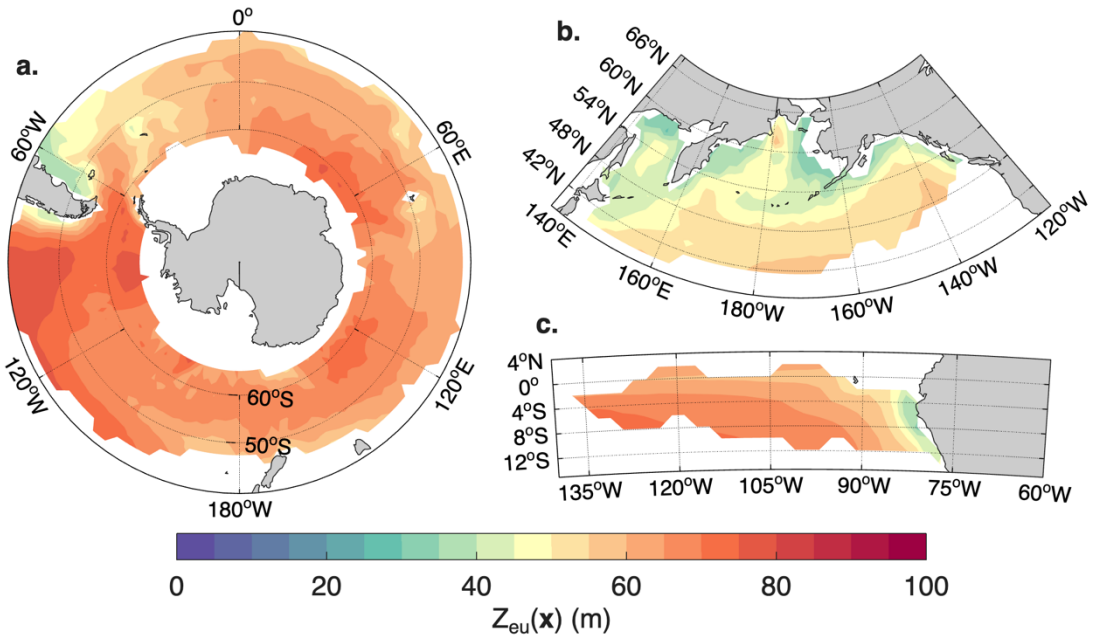


Figure S4: Spatial distribution of the annual mean depth of the euphotic zone (m), $Z_{eu}(\boldsymbol{x})$, for the OIF domain. OIF regional mean values for $Z_{eu}(\boldsymbol{x})$ are 60 m (10 m stdev.).

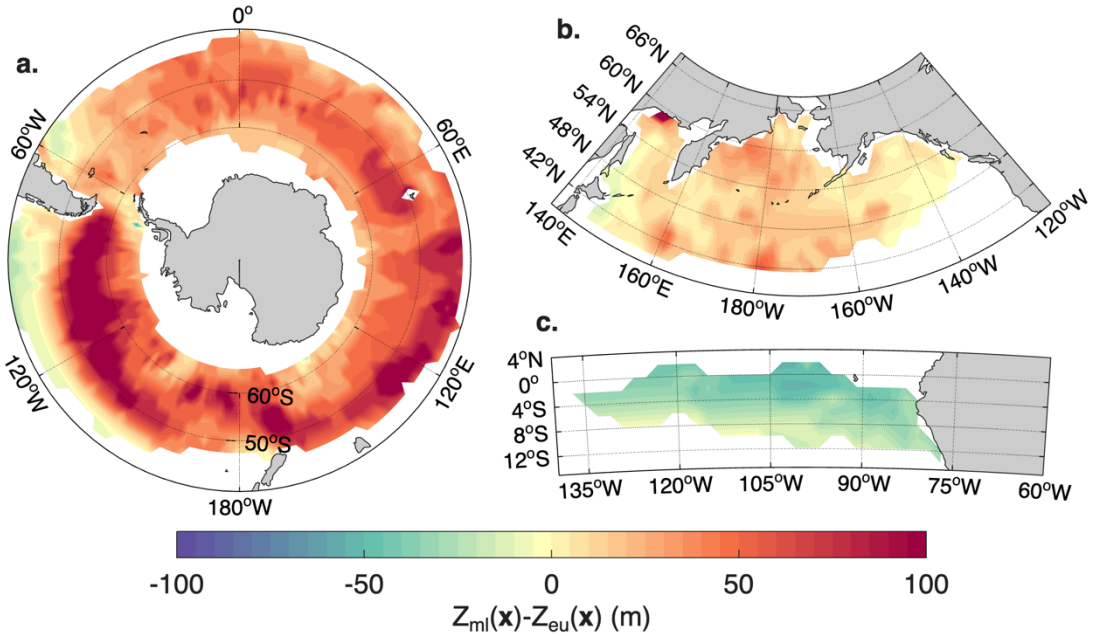


Figure S5: Spatial distribution of the difference between the depths of the annual mean mixed layer and the annual mean euphotic zone (m), $Z_{ml}(\boldsymbol{x})$ - $Z_{eu}(\boldsymbol{x})$, for the OIF domain. OIF regional mean values for $Z_{ml}(\boldsymbol{x})$ - $Z_{eu}(\boldsymbol{x})$ are 36 m (35 m stdev.).

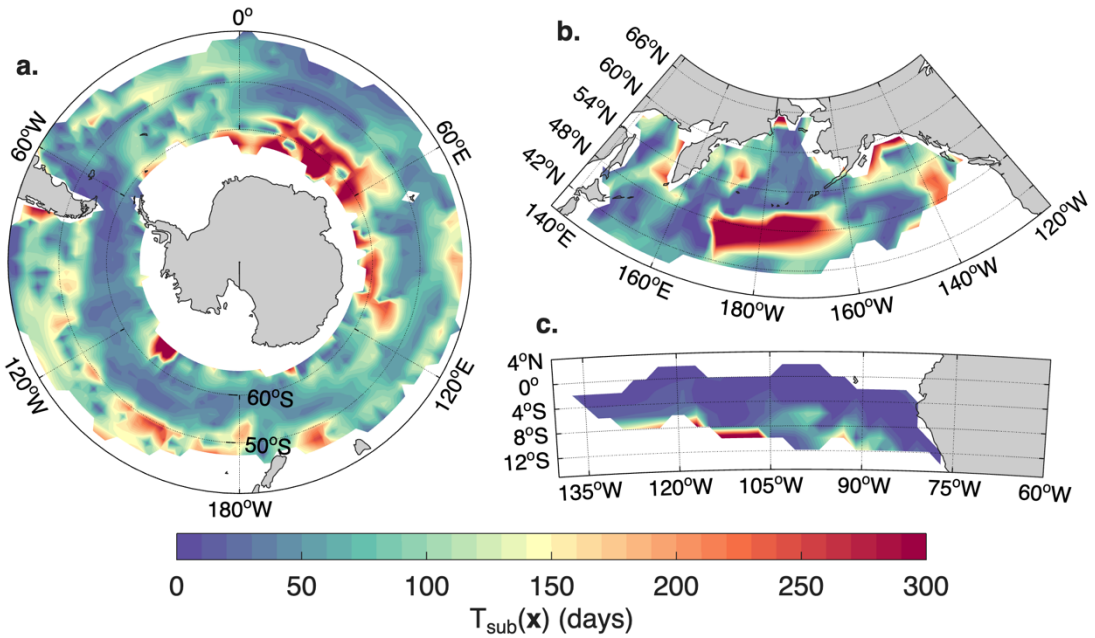


Figure S6: Mixing time scale for the mixed layer, $T_{sub}(\boldsymbol{x})$ (days) for the OIF domain. $T_{sub}(\boldsymbol{x})$ is determined as the time at which the concentration of a scalar released in the surface mixed layer is reduced by a factor of two. OIF regional mean values for $T_{sub}(\boldsymbol{x})$ are 84 (79 stdev.) days.

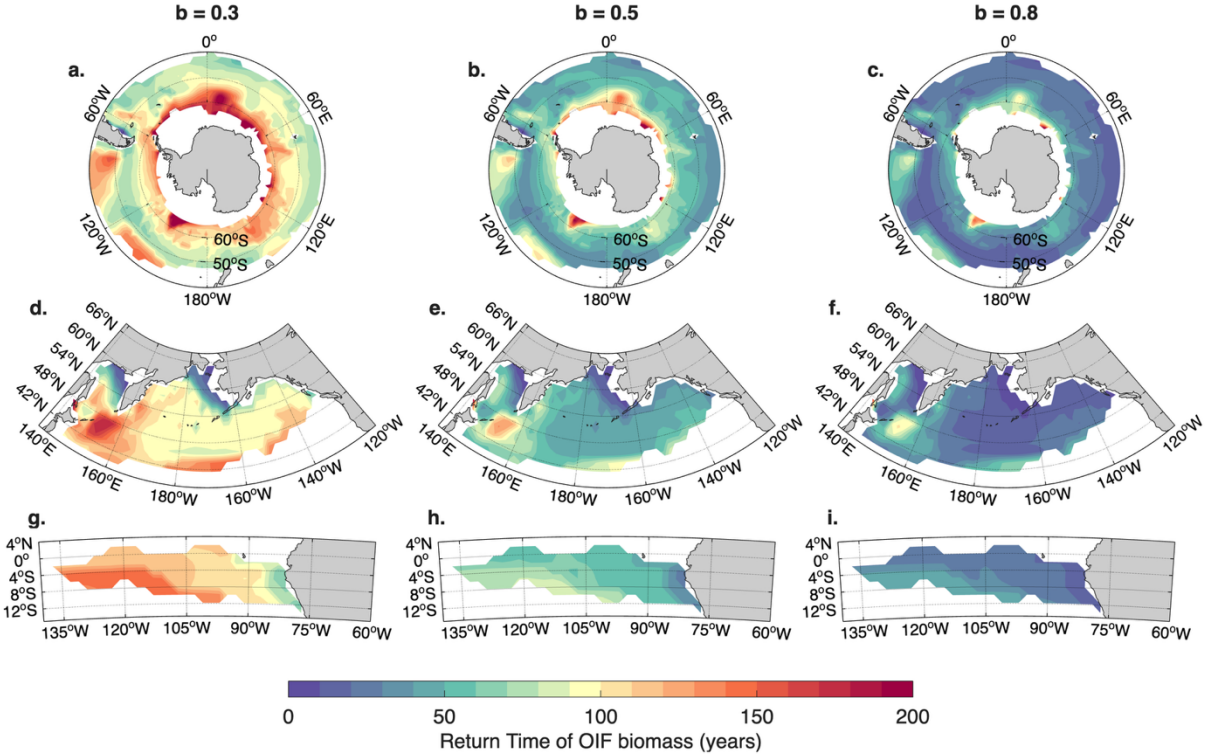


Figure S7: Spatial distribution of the mean time it takes for the remineralized OIF biomass to reach the sea surface, $T_{ret}(\boldsymbol{x},b)$. Panels are left to right b values of 0.3, 0.5 and 0.8, respectively. OIF regional mean values for $T_{ret}(\boldsymbol{x},b)$ are 106 (41), 63 (35) and 37 (28) days for b values of 0.3, 0.5 & 0.8 respectively. Values in parentheses denote domain standard deviations.

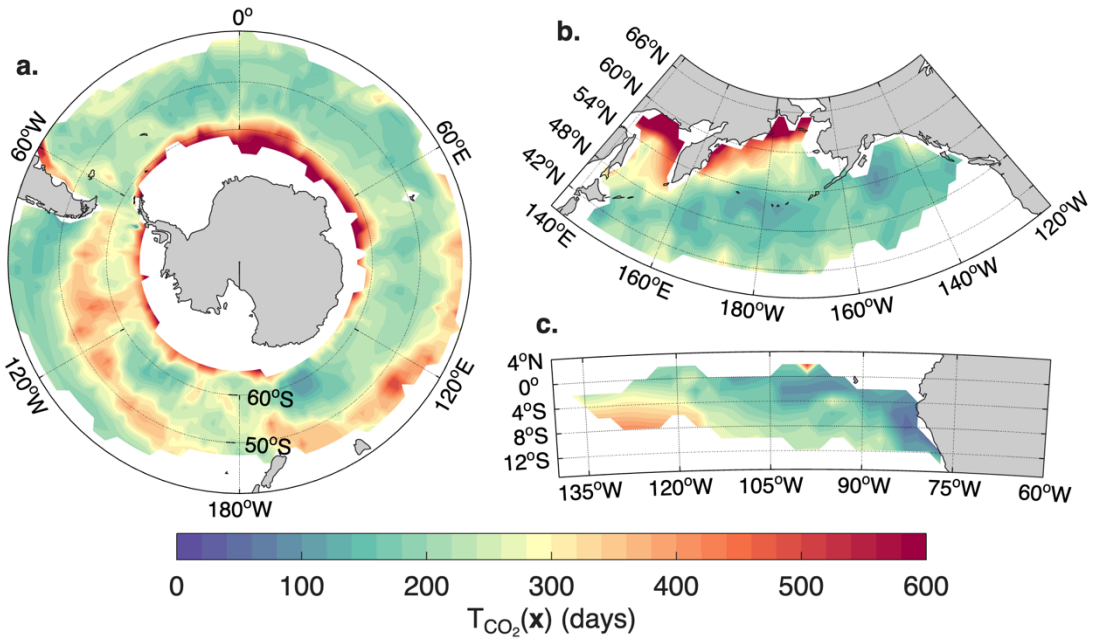


Figure S8: Air-sea exchange CO_2 equilibration timescale for the annual mean mixed layer, $T_{CO2}(\boldsymbol{x})$, (days) for the OIF domain. OIF regional mean values for $T_{CO2}(\boldsymbol{x})$ are 279 (159 stdev.) days.

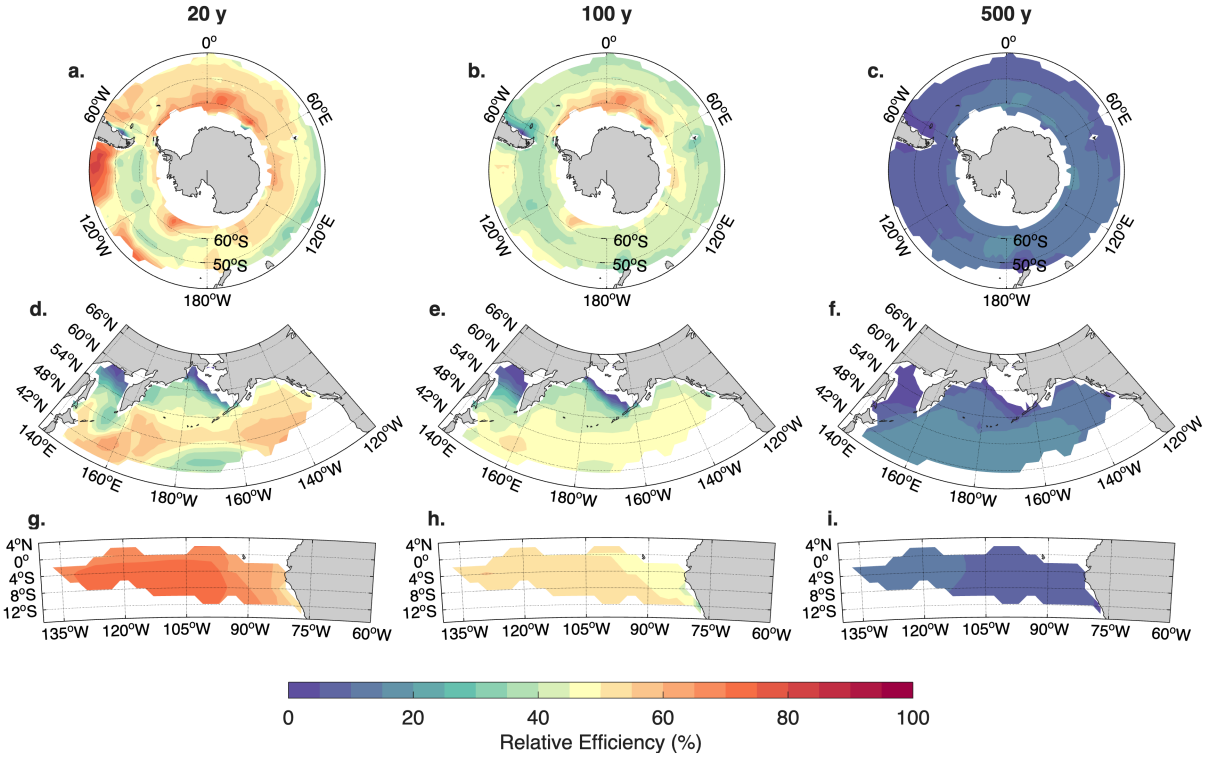


Figure S9: Relative efficiency values at 10, 100 and 500 years after the OIF CDR intervention for a Martin *b* value of 0.3 for sites in the Southern Ocean, North Pacific, and Eastern Equatorial Pacific.

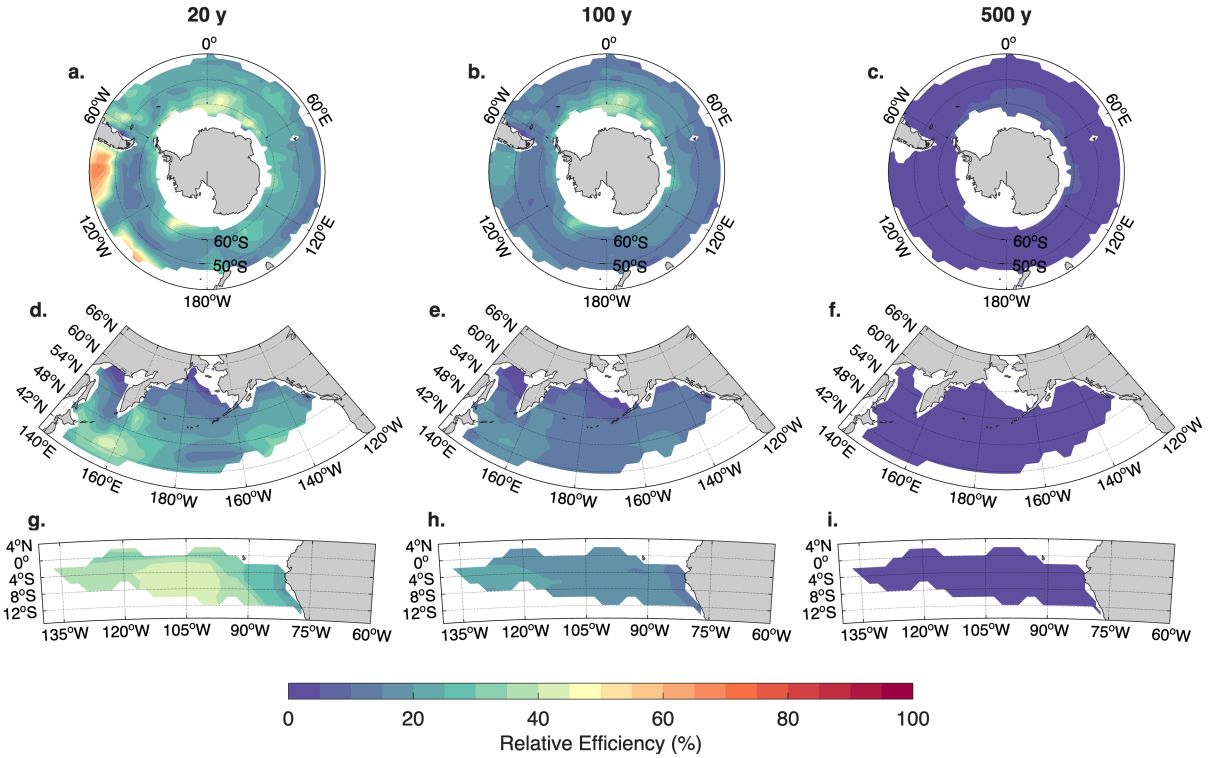


Figure S10: Relative efficiency values at 10, 100 and 500 years after the OIF CDR intervention for a Martin *b* value of 0.8 for sites in the Southern Ocean, North Pacific, and Eastern Equatorial Pacific.

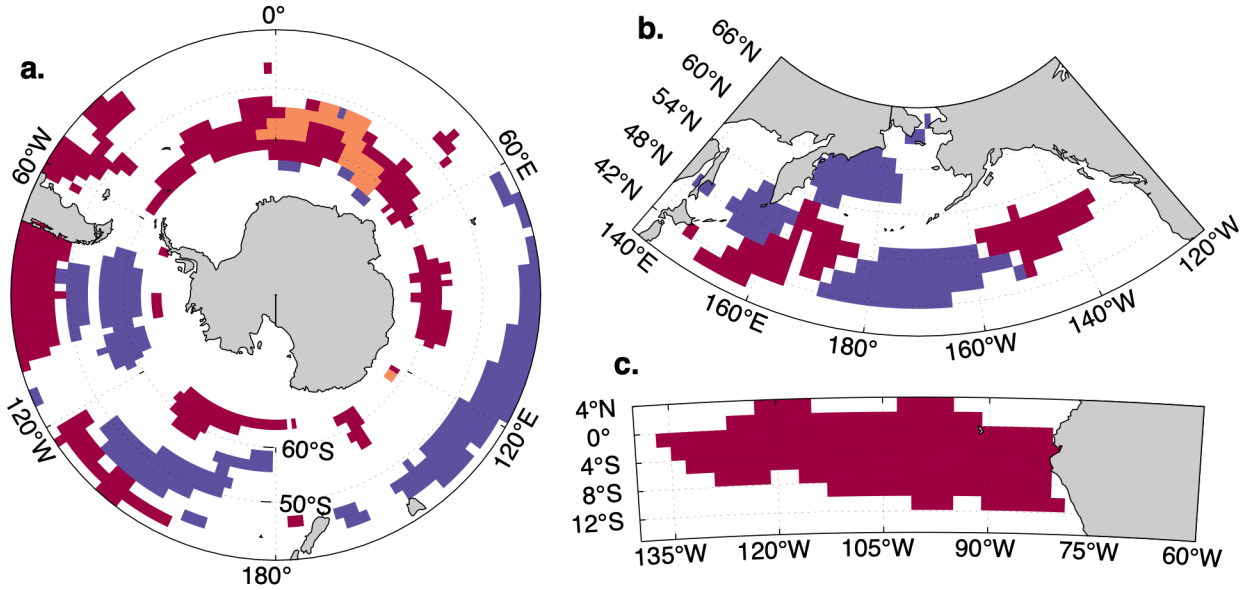


Figure S11: Locations where the best OIF CDR efficiency and durability are found for the *b* = 0.3 case. Shown are locations where the best 25% of the $\varepsilon(20, \boldsymbol{x}, 0.3)$ (red) and *DI*(***x***,0.3) (violet) are found. The orange shows regions where the highest 25% OIF efficiency and durability metrics coincide.

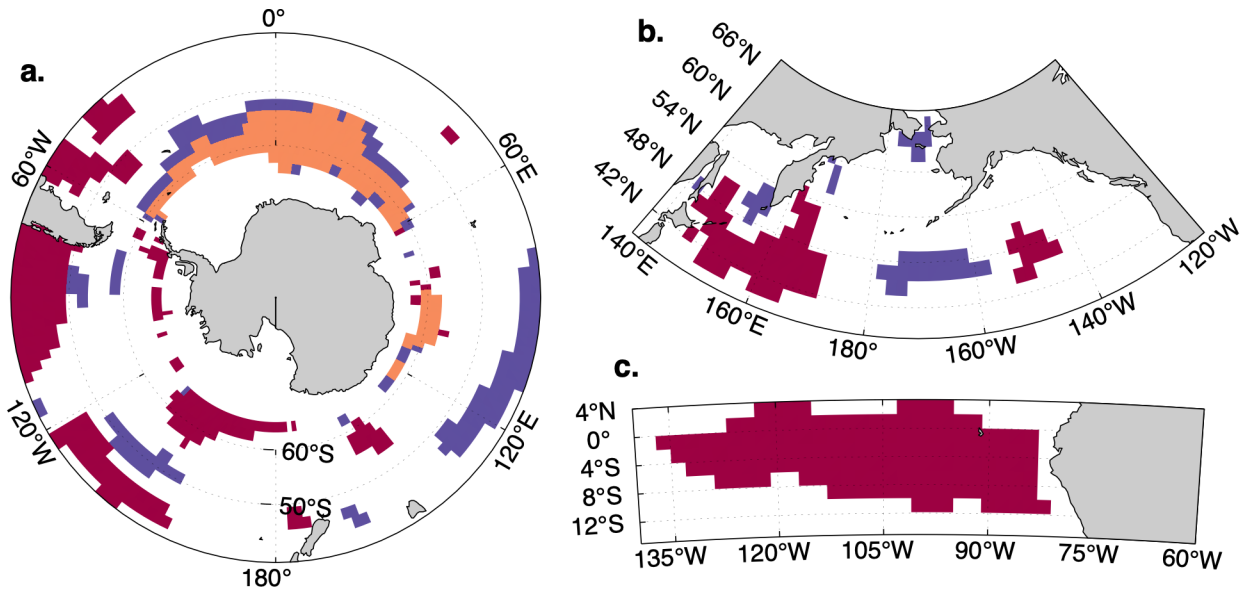


Figure S12: Locations where the best OIF CDR efficiency and durability are found for the *b* = 0.8 case. Shown are locations where the best 25% of the $\varepsilon(20, \boldsymbol{x}, 0.8)$ (red) and *DI*(***x***,0.8) (violet) are found. The orange shows regions where the highest 25% OIF efficiency and durability metrics coincide.

Table S1; Conditionally averaged mean values for important time and depth scale metrics for the b = 0.3 (upper) and b = 0.8 cases. Shown are mean values for the entire region where OIF is possible ("total"), regions where the upper ("best") and lower ("worst") quadrilles for the $\varepsilon(20, \boldsymbol{x})$ and $DI(\mathbf{x})$ values are found. Also shown are mean metrics for the intersection of the upper quadrilles for the $\varepsilon(20, \boldsymbol{x})$ and $DI(\mathbf{x})$ values.

b=0.3	T_{CO2} **(d)**	T_{sub} **(d)**	T_{remin} **(y)**	Z_{ml}-Z_{eu} **(m)**
Total OIF Region	278.7	84.4	107.5	35.9
Best ε(*x*,20)	266.9	108.5	128.1	8.2
Worst ε(*x*,20)	369.7	60.5	106.2	58.4
Best *DI*(*x*)	339.6	75.9	117.3	56.3
Worst *DI*(*x*)	252.3	68.7	95.8	12.0
Best ε(*x*,20) & *DI*(*x*)	309.2	187.1	148.6	33.2

b=0.8	T_{CO2} **(d)**	T_{sub} **(d)**	T_{remin} **(y)**	Z_{ml}-Z_{eu} **(m)**
Total OIF Region	278.7	84.4	107.5	35.9
Best ε(*x*,20)	281.5	102.6	52.6	7.4
Worst ε(*x*,20)	355.3	65.3	29.5	59.1
Best *DI*(*x*)	360.8	98.2	51.4	47.0
Worst *DI*(*x*)	246.4	71.7	33.6	5.2
Best ε(*x*,20) & *DI*(*x*)	391.6	174.7	66.3	27.6